PyIRoGlass: An Open-Source, Bayesian MCMC Algorithm for Fitting Baselines to FTIR Spectra of Basaltic-Andesitic Glasses

Sarah C. Shi[1], W. Henry Towbin[1], Terry Plank[1], Anna Barth[1,2],
Daniel Rasmussen[3], Yves Moussallam[1], Hyun Joo Lee[1],
William Menke[1]

[1]Lamont-Doherty Earth Observatory, Columbia University. New York, NY
[2]University of California, Berkeley. Berkeley, CA
[3]National Museum of Natural History, Smithsonian Institution. Washington, DC
[*]Corresponding Author (sarah.shi@columbia.edu)

The Python package can be accessed on GitHub at github.com/sarahshi/PyIRoGlass, and downloaded with PyPi. An implementation can be found on Google Colab at colab.research.google.com/github/SarahShi/PyIRoGlass/blob/main/PyIRoGlass_RUN_colab.ipynb. If you encounter any issues, please reach out or raise an issue on GitHub. We welcome constructive feedback.

PyIRoGlass: An Open-Source, Bayesian MCMC Algorithm for Fitting Baselines to FTIR Spectra of Basaltic-Andesitic Glasses

Sarah C. Shi *[α], W. Henry Towbin[α], Terry Plank[α], Anna Barth[α,β], Daniel Rasmussen[α,γ], Yves Moussallam[α], Hyun Joo Lee[α], and William Menke[α]
[α]Lamont-Doherty Earth Observatory, Columbia University. New York, NY USA
[β]University of California, Berkeley. Berkeley, CA USA
[γ]National Museum of Natural History, Smithsonian Institution. Washington, DC USA

ABSTRACT

Quantifying volatile concentrations in magmas is critical for understanding magma storage, phase equilibria, and eruption processes. We present PyIRoGlass, an open-source Python package for quantifying H_2O and CO_2 species concentrations in the transmission FTIR spectra of basaltic to andesitic glasses. We leverage a database of naturally degassed melt inclusions and back-arc basin basalts to delineate the fundamental shape and variability of the baseline underlying the CO_3^{2-} and $H_2O_{m,1635}$ peaks, in the mid-infrared region. All Beer-Lambert Law parameters are examined to quantify associated uncertainties. PyIRoGlass employs Bayesian inference and Markov Chain Monte Carlo sampling to fit all probable baselines and peaks, solving for best-fit parameters and capturing covariance to offer robust uncertainty estimates. Results from PyIRoGlass agree with independent analysis of experimental devolatilized glasses (within 6%) and interlaboratory standards (13% for H_2O, 9% for CO_2). The open-source nature of PyIRoGlass ensures its adaptability and evolution as more data become available.

KEYWORDS: Volatiles; Ftir; Open-source; Python; Bayesian; Markov chain monte carlo.

1 INTRODUCTION

The loss of volatiles from magma during exsolution and degassing modulates phase equilibria [Sisson and Grove 1993], crystallinity [Blundy and Cashman 2001], density [Ochs III and Lange 1999], and viscosity [Hess and Dingwell 1996] from magma genesis to eruption. Major volatile components are H_2O and CO_2, both of which have strong pressure-dependent solubilities. Analyses of H_2O and CO_2 in mineral-hosted melt inclusions are often utilized to estimate the conditions of magma storage and evolution, whereas analyses of synthetic glasses inform understandings of solubility and phase equilibria. H_2O and CO_2 in volcanic glasses and synthetic products are commonly measured with two analytical techniques: Fourier Transform Infrared Spectroscopy (FTIR) and Secondary-Ion Mass Spectrometry (SIMS). Here we focus on the FTIR technique, with the goal of improving the fitting of baselines and peaks in FTIR spectra and quantifying uncertainties in the resulting concentrations.

FTIR spectroscopy utilizes infrared light to excite materials, where infrared absorbance relates to the rotational, vibrational, and electronic energies of molecular bonds. Absorbance is proportional to concentration, allowing for the quantification of species with the Beer-Lambert Law:

$$c = \frac{AM}{\varepsilon l \rho} \tag{1}$$

where c is concentration, A is absorbance, M is the molar mass of the absorbing volatile species (g·mol^{-1}), ε is the absorptivity of the species (L·mol^{-1}·m), l is the optical path length or thickness (m), and ρ is density (kg·m^{-3}). H_2O and CO_2 species in silicate glasses absorb light in the near-infrared (12800-4000 cm^{-1}) and mid-infrared (4000-200 cm^{-1}) wavenumber regions (Figure 1). Volatile species vibration is observed through absorbance, with the vibrations occurring as bending or stretching.

Dissolution of H_2O in silicate liquids forms both molecular water (H_2O_m) and hydroxyl (OH^-) species with concentration dependence. The vibration of H_2O species combines bending and stretching energies in two dimensions [von Aulock et al. 2014]. Two H_2O_m peaks are found at ~5200 and ~1635 cm^{-1}, and one OH^- peak is found at ~4500 cm^{-1} (Figure 1). Total H_2O (H_2O_t) is represented by the ~3550 cm^{-1} peak. Linear relationships between absorbance and concentration dominate, but non-linear relationships can be introduced when increased sample thicknesses result in insufficient light transmission to the detector, causing the $H_2O_{t,3550}$ peak to saturate with ragged peak tops and absorbances exceeding 2 [von Aulock et al. 2014; McIntosh et al. 2017]. When $H_2O_{t,3550}$ is saturated, the combination of $H_2O_{m,5200}$ or $H_2O_{m,1635}$ with OH^-_{4500} species must be used instead. Dissolution of CO_2 forms carbonate (CO_3^{2-}) and molecular carbon dioxide (CO_2). The vibration of CO_2 species combines bending and stretching in three dimensions [von Aulock et al. 2014]. The CO_2 peak occurs at ~2350 cm^{-1} and the CO_3^{2-} doublet occurs at ~1515 and ~1430 cm^{-1} (Figure 1). We restrict our treatment to basaltic to andesitic glasses, where the CO_3^{2-} species dominate [Dixon and Pan 1995; Brooker et al. 2001a; b; Lowenstern 2001].

The determination of volatile concentrations in silicate glasses requires the measurement of peak heights or areas, defined as the difference in absorbance or integrated absorbance between peak and baseline. Variability and subjectivity in baseline definition constitutes a significant, and typically unreported, uncertainty in most studies determining volatile concentrations. The $H_2O_{m,5200}$, OH^-_{4500}, and $H_2O_{t,3550}$ peaks in

---

* ✉ sarah.shi@columbia.edu

the near-infrared to mid-infrared region can be well quantified with linear to near-linear baselines between the two absorbance minima on either side of the peak. The $H_2O_{m,1635}$ peak and CO_3^{2-} doublet peaks pose greater challenges due to the steep and sharp increase of baseline absorbance at wavenumbers lower than 1430 cm^{-1}. The convolution of the tails of the $H_2O_{m,1635}$ peak and the $CO^{2-}_{3,1515}$ doublet peak in glass spectra is a further complication. Devolatilized glass baselines are the gold standard but are not possible to apply in melt inclusion studies, where large pieces of glass are not readily available. Previous studies have approximated baselines beneath the $H_2O_{m,1635}$ and CO_3^{2-} doublet peaks using the spectra of chemistry- and matrix-matched devolatilized glasses [Dixon et al. 1988; Newman et al. 2000], splines and flexicurves [Dixon and Stolper 1995], and other curve functions [Dixon and Clague 2001]. Such approaches are highly subjective, difficult to reproduce, and seldom reported with uncertainties. The main motivation in our development of PyIRoGlass is to provide an open-source code that reproducibly fits transmission FTIR baselines and peaks with quantified uncertainties.

2 COMPONENTS OF PYIROGLASS

We examine each free parameter within the Beer-Lambert Law (A, ε, l, ρ) to develop PyIRoGlass, a Python implementation of a Bayesian algorithm with Markov Chain Monte Carlo (MCMC) sampling for fitting baselines and peaks for all H_2O and CO_2 species in basaltic to andesitic glasses. There are several components to PyIRoGlass:

I. **Section 2.1** Absorbance (A): We assess the fundamental shape and variability of the infrared baseline using principal component analysis (PCA) applied to a database of absorbance spectra for naturally degassed melt inclusions from the Aleutian arc [Rasmussen 2019] and back-arc basin glasses [Pearce et al. 1994], relevant for basaltic to andesitic silicate melts. Application of PCA to a training dataset of spectra with volatiles below detection allows for the assessment of the fundamental shape of the baseline and the spectral features contributing to its variability [Carvajal et al. 2016].

II. **Section 2.2** Molar Absorptivity (ε): We refit the relationships between molar absorptivity and composition with implicit iterative inversions, updating the parameterization of Mandeville et al. [2002] with new data, to derive molar absorptivity with uncertainty.

III. **Section 2.3** Thickness (l), Density (ρ): To calculate thickness, we develop automated implementations using the reflectance FTIR interference fringe method [Nishikida et al. 1996; Tamic et al. 2001; Wysoczanski and Tani 2006; Sun et al. 2007]. Because glass density is significantly affected by H_2O concentration, we outline an iterative approach to calculating density and H_2O concentration together.

IV. **Section 2.4** PyIRoGlass integrates all the above steps by employing a Bayesian algorithm with Markov Chain Monte Carlo sampling to find best-fit spectral baselines and peaks, given inputs of the infrared spectrum, thickness, and composition (to calculate molar absorptivity). The output of PyIRoGlass consists of peak heights and concentrations calculated from the Beer-Lambert Law (Equation 1) for each CO_2 and H_2O peak, with their uncertainties.

2.1 Assessing Variability in Baselines and Peaks

We consider two different approaches to estimating baselines and extracting peak heights. Baselines for the $H_2O_{m,5200}$, OH^-_{4500}, and $H_2O_{t,3550}$ peaks are nominally linear (Figure 1), so we use an asymmetric least squares method to determine the baseline, further discussed in Section *2.1.1*. In the wavenumber region between 2400 and 1250 cm^{-1}, the baseline has a complex shape beneath the $H_2O_{m,1635}$ peak and the CO_3^{2-} doublet (1515 and 1430 cm^{-1}). Moreover, the tail on the $H_2O_{m,1635}$ peak can convolute with the $CO^{2-}_{3,1515}$ peak. We thus develop an empirical model for the baseline and peaks in this region, based on a dataset of degassed natural glasses, described in Section *2.1.2*.

2.1.1 *Asymmetric Least Squares Baselines for $H_2O_{m,5200}$, OH^-_{4500}, and $H_2O_{t,3550}$ Peaks*

The $H_2O_{t,3550}$, $H_2O_{m,5200}$, and OH^-_{4500} baselines are fit with the asymmetric least squares (ALS) method [Eilers 2004]. ALS iteratively solves for interpolated baseline fittings, balancing smoothness and asymmetry while remaining fast, and is commonly used in the processing of Raman and infrared spectra [Eilers 2004; Peng et al. 2010; Lee et al. 2017]. Data are preprocessed by first applying a median filter to remove single spike noise. We vary the peak fitting region surrounding each peak and fit three repeat baselines with ALS to assess uncertainty within the peak shape and location. The baselines are subtracted from the peak. The three baseline-subtracted peaks are processed with kriging interpolation to reduce noise and to obtain maximum peak height [Krige 1951]. Kriging interpolation utilizes sample data of limited resolution to predict and interpolate data of higher resolution with estimates of uncertainty in each interpolated value. The mean peak absorbance and standard deviation in absorbance are determined from the three baseline-subtracted peaks. $H_2O_{t,3550}$ saturation prompts the return of an error message and suggests the use of the $H_2O_{m,1635}$ and OH^-_{4500} peaks for determining H_2O_t. The use of the $H_2O_{m,1635}$ over the $H_2O_{m,5200}$ peak is further discussed in Section 3.4.

2.1.2 *Baselines for the $H_2O_{m,1635}$, $CO^{2-}_{3,1515}$, and $CO^{2-}_{3,1430}$ Peaks*

The compositional variability and small size of melt inclusions (often <100 µm) present challenges for determining FTIR baselines for the $H_2O_{m,1635}$ and CO_3^{2-} doublet. While FTIR spectra of devolatilized glasses are one of the best ways to determine baselines for the complex spectral region underlying the peaks, these glasses unfortunately do not exist for all melt inclusion compositions. The approach we have taken is to use naturally degassed melt inclusions and back-arc basin (BAB) glasses to determine a family of baseline shapes in this spec-

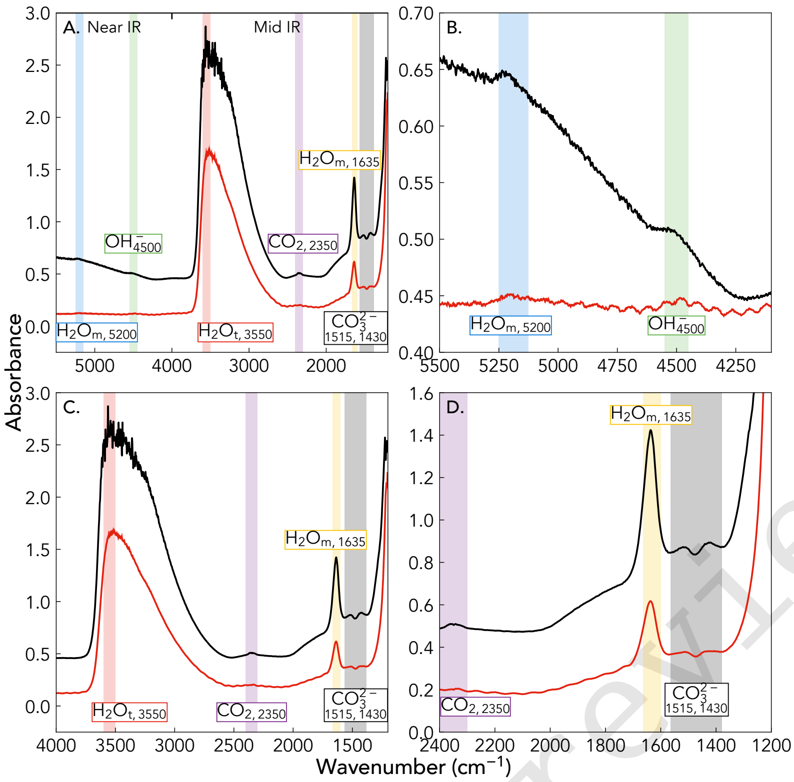

Figure 1: Example transmission FTIR spectra of olivine-hosted melt inclusions VF18-AC4-OL49 (black) and VF18-AC4-OL53 (red), from Volcán de Fuego, Guatemala (see Section 3.2) OL49 is 91±3 µm thick and OL53 is 39±3 µm thick. Greater thicknesses increase absorbance and contribute to saturation, seen when the absorbance of $H_2O_{t,3550}$ exceeds 2 and the peak is ragged. A. Transmission FTIR spectra through near-IR and mid-IR regions. B. $H_2O_{m,5200}$ and OH^-_{4500} peaks in the near-IR region. OL53's absorbance spectrum is shifted upwards for visualization. OL49 has strong signal-to-noise ratios with well-defined peaks, but OL53 has low signal-to-noise ratios with interference fringes. Saturated samples have high signal-to-noise ratio peaks in the near-IR region. OL49 contains 1.81±0.35 wt.% $H_2O_{m,5200}$ and 1.25±0.26 wt.% OH^-_{4500}. OL53's near-IR peaks are not considered given lack of saturation. C. $H_2O_{t,3550}$ peak. OL49 is saturated in $H_2O_{t,3550}$, introducing non-linearity into the Beer-Lambert Law and preventing usage. OL53 contains 4.03±0.43 wt.% $H_2O_{t,3550}$. D. $H_2O_{m,1635}$ peak and CO_3^{2-} doublet. Rapid absorbance upturn following the $CO^{2-}_{3,1430}$ peak prevents a linear baseline from being fitted, motivating the development of PyIRoGlass. OL49 contains 1.30±0.19 wt.% $H_2O_{m,1635}$ and 749±37 ppm CO_2 and OL53 contains 1.49±0.26 wt.% $H_2O_{m,1635}$ and 728±62 ppm CO_2, with concentrations processed from PyIRoGlass.

tral region. Degassed melt inclusions are typically considered failures in the attempt to characterize the volatile concentrations of magmas. We make use of a dataset of failures here to define baseline shapes for natural basalts and andesites, with raw spectra shown in Figure 2. The dataset consists of 55 transmission FTIR spectra of Aleutian melt inclusions [Rasmussen 2019] and back-arc basin glasses [Newman et al. 2000] that span a compositional range from basalt to andesite (SiO_2 = 43-60 wt.%, TiO_2 = 0.7-5.4 wt.%, Al_2O_3 = 10.9-20.8 wt.%, FeO = 6.3-22.2 wt.%, MgO = 2.1-7.0 wt.%, CaO = 4.3-15.6 wt.%, Na_2O = 2.2-4.4 wt.%, K_2O = 0.2-1.9 wt.%). Some spectra were lacking both detectable $H_2O_{m,1635}$ and CO_3^{2-} peaks (n = 14), while others had $H_2O_{m,1635}$ with no detectable CO_3^{2-} peaks (n = 41).

Definition of baseline and peak shapes is iterative. First, we use the degassed (volatiles below detection) absorbance spectra to generate an initial mean baseline or $\overline{\text{Baseline}_i}$ (Figure 2A). Spectra are shifted and scaled to ensure equal absorbance in the wavenumber fitting range from 2400 to 1250 cm^{-1}. We describe variability within the baseline with principal component analysis (PCA). Four principal components (PC) describe more than 95% of the variance within the initial baseline.

Next, we use the spectra containing $H_2O_{m,1635}$ but with CO_3^{2-} below detection to both define peak shapes and to create a greater number of baselines. Spectra with $H_2O_{m,1635}$ but with CO_3^{2-} below detection are first fit for the $H_2O_{m,1635}$ peak, then stripped of it (Figure 2B). We fit the spectra with $\overline{\text{Baseline}_i}$ and four principal components to isolate the shape of the $H_2O_{m,1635}$ peak, which is neither Gaussian nor Lorentzian, due to the rapid downturn of the $H_2O_{m,1635}$ peak. We thus identify the mean $H_2O_{m,1635}$ peak ($\overline{H_2O_{m,1635}}$) and describe variability within the peak with PCA (Figure 2C, Figure 2F). The first two principal components of $\overline{H_2O_{m,1635}}_{PC1-2}$ accommodate variations in $H_2O_{m,1635}$ peak shape and location from its nominal peak location of 1635 cm^{-1}. $\overline{H_2O_{m,1635}}_{PC1}$ is similar to the negative second derivative of the $H_2O_{m,1635}$ peak; $\overline{H_2O_{m,1635}}_{PC2}$ is similar to the

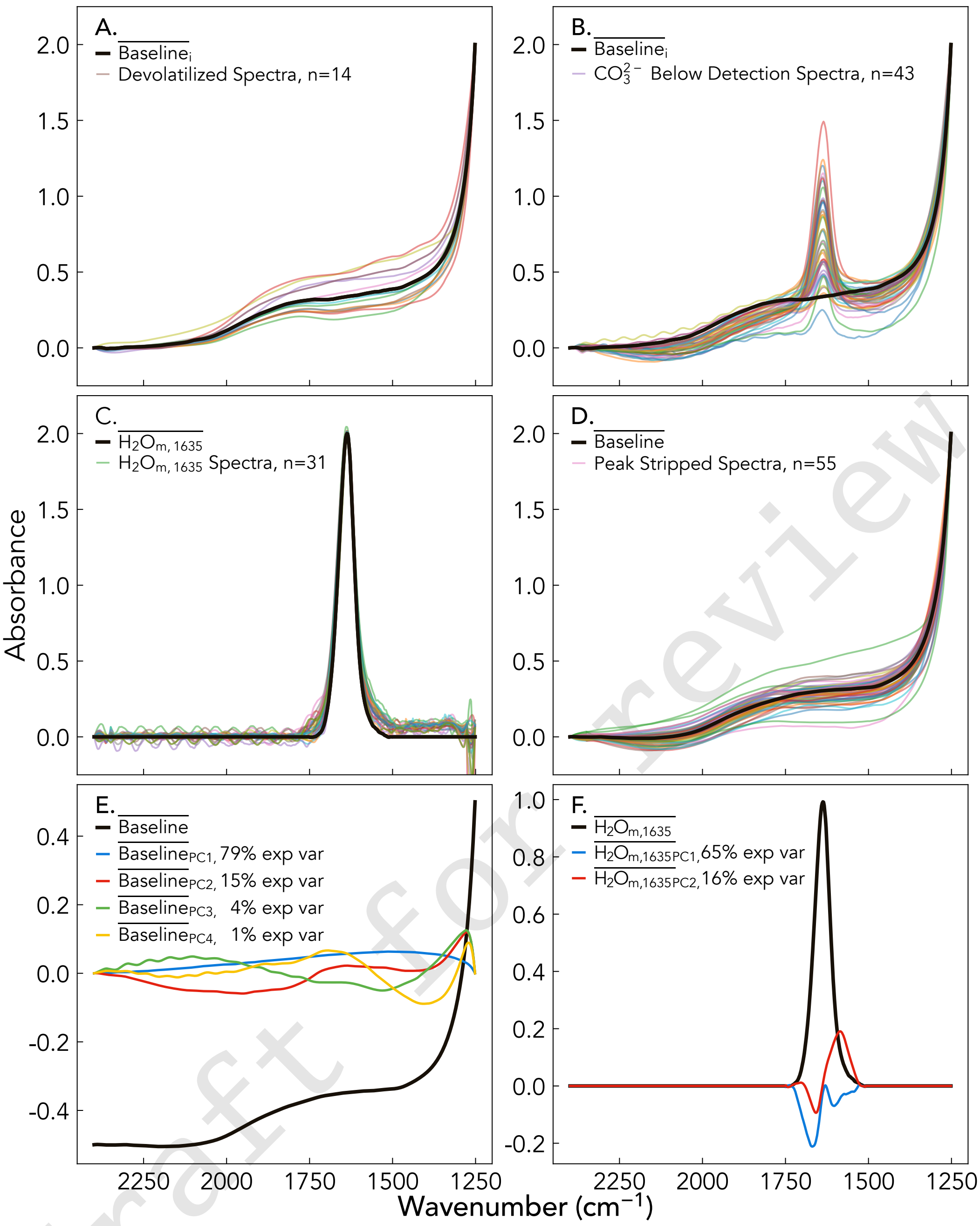

Figure 2: Transmission FTIR spectra for the dataset of degassed basaltic to andesitic melt inclusions and glasses used to identify the range of possible baselines for fitting $H_2O_{m,1635}$, $CO^{2-}_{3,1515}$, and $CO^{2-}_{3,1430}$ peaks. A. Absorbance spectra in the naturally degassed dataset used to generate initial mean baseline, $\overline{\mathrm{Baseline_i}}$ (black). Spectra are linearly rescaled to span an absorbance range of 0-2 in the wavenumber fitting range of 2400 to 1250 cm^{-1}. B. Absorbance spectra with CO_3^{2-} below detection are fit with $\overline{\mathrm{Baseline_i}}$ in a least squares optimization to identify the $H_2O_{m,1635}$ peak shape, allowing for peak-stripping to generate synthetically 'degassed' spectra. These spectra are similarly linearly rescaled in the wavenumber fitting range. High wavenumber fringes likely represent internal reflections in transmission FTIR. C. $H_2O_{m,1635}$ peaks identified by least squares baseline subtraction are used to generate the mean $H_2O_{m,1635}$ ($\overline{H_2O_{m,1635}}$) peak shape and two associated principal components of $\overline{H_2O_{m,1635}}_{PC1-2}$. D. The full degassed dataset following peak-stripping of absorbance spectra, using least squares fitting of $\overline{H_2O_{m,1635}}$ and $\overline{H_2O_{m,1635}}_{PC1-2}$. These spectra generate the final mean baseline ($\overline{\mathrm{Baseline}}$) and four associated principal components of $\overline{\mathrm{Baseline}}_{PC1-4}$ shown in panel E. E. $\overline{\mathrm{Baseline}}$ and $\overline{\mathrm{Baseline}}_{PC1-4}$ describing variability in the baseline, text shows percentage of the variance explained by that principal component (exp var). F. $\overline{H_2O_{m,1635}}$ and $\overline{H_2O_{m,1635}}_{PC1-2}$ describing variability in the peak. $\overline{H_2O_{m,1635}}_{PC1}$ is similar to the negative second derivative and $\overline{H_2O_{m,1635}}_{PC2}$ is similar to the first derivative of the $\overline{H_2O_{m,1635}}$ peak.

first derivative of the $H_2O_{m,1635}$ peak. We restricted our analysis to the first two principal components, which accounted for over 80% of the variance within the peak shape. Subsequent principal components introduced considerable noise and were therefore excluded. Identification of the $H_2O_{m,1635}$ peak shape further allows for $H_2O_{m,1635}$ peak subtraction from the spectra with CO_3^{2-} below detection with least squares, generating additional degassed spectra. Spectra with CO_3^{2-} below detection are thus converted to fully degassed spectra (Figure 2D).

We iteratively identify and define the mean degassed baseline ($\overline{\mathrm{Baseline}}$) with associated variability described by addition or subtraction of four principal components of $\overline{\mathrm{Baseline}}_{\mathrm{PC1-4}}$ (Figure 2E, Figure 3). For samples that contain both $H_2O_{m,1635}$ and CO_3^{2-}, we disentangle the convoluted tails of the overlapping $H_2O_{m,1635}$ and the $CO_{3,1515}^{2-}$ peaks by identifying $\overline{H_2O_{m,1635}}$ with $\overline{H_2O_{m,1635}}_{\mathrm{PC1-2}}$ and the Gaussian CO_3^{2-} peaks. Given the sharp upturn in absorbance while approaching 1250 cm^{-1}, we provide additional accommodation for shifting and tilting the $H_2O_{m,1635}$ peak and CO_3^{2-} doublet with a linear shift.

We can therefore describe the range of possible degassed baselines while simultaneously fitting peaks appropriate for basaltic to andesitic glasses with the net equation:

$$\hat{\mathrm{A}} = \hat{\mathrm{B}} + \widehat{H_2O_{m,1635}} + \widehat{CO_3^{2-}} + \hat{\mathrm{L}}, \tag{2}$$

where $\hat{A}$ is the best-fit absorbance spectrum.

$\hat{B}$, the best-fit baseline, is fit by:

$$\hat{\mathrm{B}} = x_0\overline{\mathrm{B}} + x_1\overline{\mathrm{B}}_{\mathrm{PC1}} + x_2\overline{\mathrm{B}}_{\mathrm{PC2}} + x_3\overline{\mathrm{B}}_{\mathrm{PC3}} + x_4\overline{\mathrm{B}}_{\mathrm{PC4}}, \tag{3}$$

where the x_n terms are best-fit scaling parameters, $\overline{\mathrm{B}}$ is the mean baseline, and $\overline{\mathrm{B}}_{\mathrm{PCn}}$ is the n-th principal component of the baseline.

$\widehat{H_2O_{m,1635}}$, the best-fit $H_2O_{m,1635}$ peak, is fit by:

$$\begin{aligned}\widehat{H_2O_{m,1635}} = {} & y_0\overline{H_2O_{m,1635}} + y_1\overline{H_2O_{m,1635}}_{\mathrm{PC1}} \\ & + y_2\overline{H_2O_{m,1635}}_{\mathrm{PC2}},\end{aligned} \tag{4}$$

where the y_n terms are best-fit scaling parameters, $\overline{H_2O_{m,1635}}$ is the mean $H_2O_{m,1635}$ peak, and $\overline{H_2O_{m,1635}}_{\mathrm{PCn}}$ is the n-th principal component of the $H_2O_{m,1635}$ peak. The $\overline{H_2O_{m,1635}}$ term fits peak amplitude and the $\overline{H_2O_{m,1635}}_{\mathrm{PC1-2}}$ terms accommodate lateral variations in peak location. $\widehat{CO_3^{2-}}$, the best-fit CO_3^{2-} peak, is fit by:

$$\widehat{CO_3^{2-}} = \frac{a}{2\sigma^2} \cdot e^{-(\upsilon^- - \mu)^2}, \tag{5}$$

where a is the peak amplitude, σ is the peak half-width, υ^- is the fitting wavenumber range, and μ is the central wavenumber of the peak. The μ parameter allows for slight deviations (± 14 cm^{-1}) in peak location.

$\hat{L}$, a linear function allowing for tilt and vertical offset of the whole spectrum, is described by:

$$\hat{L} = m\upsilon^- + b \tag{6}$$

where m is the slope, υ^- is the wavenumber range of interest, and b is the intercept.

Peak and baseline parameters are sampled and fit concurrently within an MCMC framework with Bayesian inference to accounts for uncertainties and covariance. The best-fit peak amplitudes and uncertainties for the $H_2O_{m,1635}$ and CO_3^{2-} doublet peaks are exported from the algorithm and used to determine volatile concentrations with uncertainties.

2.2 Calibrating Molar Absorptivity or Extinction Coefficient

Molar absorptivities or extinction coefficients (ε) determine the intensity at which light attenuates when passing through a material, relating absorbance to concentration. Calibration of ε involves pairing measurements of transmission FTIR absorbance spectra with H_2O or CO_2 concentrations determined by an independent volatile analytical technique. ε is dependent on glass composition — the ε related to H_2O species is dependent on the tetrahedral cation fraction of $\tau = (Si^{4+}+Al^{3+})/(\text{total cations})$ and the ε related to CO_2 is dependent on the cation fraction of $Na^+/(Na^++Ca^{2+})$, which we will term η. ε data are drawn from studies with independent methods of volatile measurement, such as elemental analyzer (EA), elastic recoil detection analysis (ERDA), experimental mass balance, Karl Fischer titration (KFT), manometry, nuclear magnetic resonance (NMR), nuclear reaction analysis (NRA), secondary-ion mass spectrometry (SIMS), and vacuum heating. We compile a new dataset of calibrated ε from studies performed between 1982 to 2023 (Table 1). In the full dataset, τ spans the range of 0.50-0.90 and η spans 0.23-0.84. We examine whether these compositional parameters remain the best descriptors of ε. We refit the linear relationships between $\varepsilon H_2O_{m,5200}$, εOH^-_{4500}, $\varepsilon H_2O_{t,3550}$, $\varepsilon H_2O_{m,1635}$, and εCO_3^{2-} and their corresponding compositional parameters using a Newtonian inversion technique. This inclusion of more recent data and broader compositional ranges was done following the last compilations of ε by Mandeville et al. [2002] and η by Dixon and Pan [1995].

ε related to H_2O species increases with τ, reflecting increased polymerization of the glass [Stolper 1982]. Tetrahedral cations have also been proposed to compete with non-tetrahedral cations ($M = Mg^{2+}, Ca^{2+}, Na^+$) to bond with free hydroxyl groups in melt [Pandya et al. 1992; Mercier et al. 2010]. More depolymerized melts will have higher proportions of free hydroxyl, which translates to more $M\text{-}(OH)_x$ bonding and hydrogen bonding [Xue 2009; Mercier et al. 2010]. Dixon et al. [1995] and Mandeville et al. [2002] demonstrate the dependence of the $\varepsilon H_2O_{m,5200}$, εOH^-_{4500}, and $\varepsilon H_2O_{m,1635}$ on glass τ. $\varepsilon H_2O_{t,3550}$ is also positively correlated with τ, but this relationship is less straightforward than originally thought [Mercier et al. 2010]. Quench temperatures and rates drive the formation of variable proportions of H_2O_m and OH^- [Silver and Stolper 1989; Stolper 1989]. $\varepsilon H_2O_{t,3550}$ is thus considered as a combination of two endmember molar absorptivities, εOH^-_{3550} and $\varepsilon H_2O_{m,3550}$, multiplied by the relative proportion of each respective species [Newman et al. 1986; Okumura et al. 2003; McIntosh et al. 2017]. Studies quantifying εOH^-_{3550} and $\varepsilon H_2O_{m,3550}$ are the gold standard, but are currently limited in compositional range. McIntosh et al. [2017]

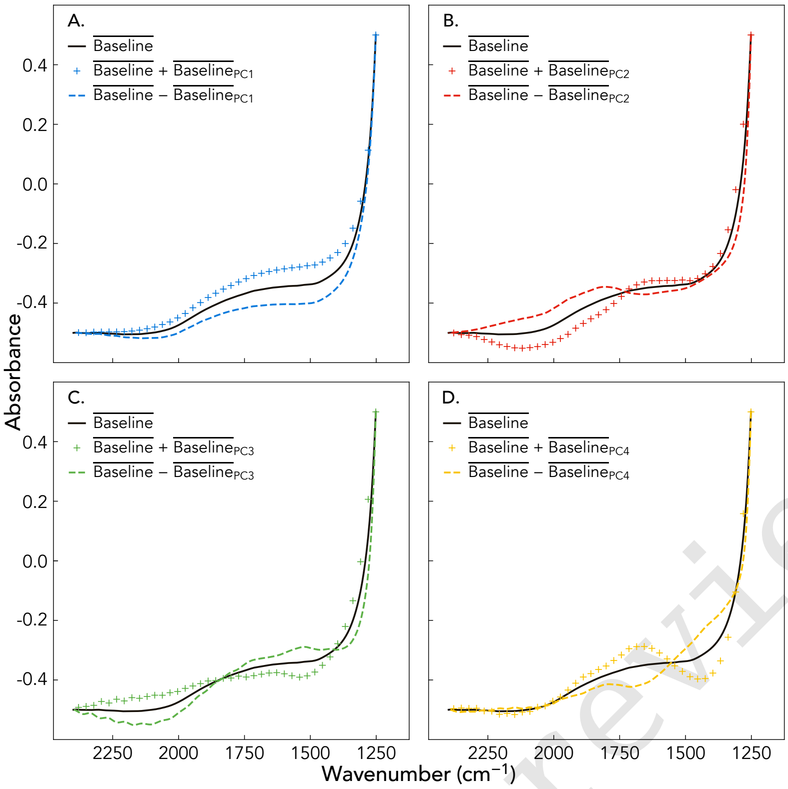

Figure 3: Mean degassed baseline ($\overline{\text{Baseline}}$) with $\overline{\text{Baseline}}_{PC1-4}$ describing variability within the baseline. A. $\overline{\text{Baseline}}\pm\overline{\text{Baseline}}_{PC1}$ most closely resembles the range of baselines in Figure 2D. B. $\overline{\text{Baseline}}\pm\overline{\text{Baseline}}_{PC2}$. C. $\overline{\text{Baseline}}\pm\overline{\text{Baseline}}_{PC3}$. D. $\overline{\text{Baseline}}\pm\overline{\text{Baseline}}_{PC4}$.

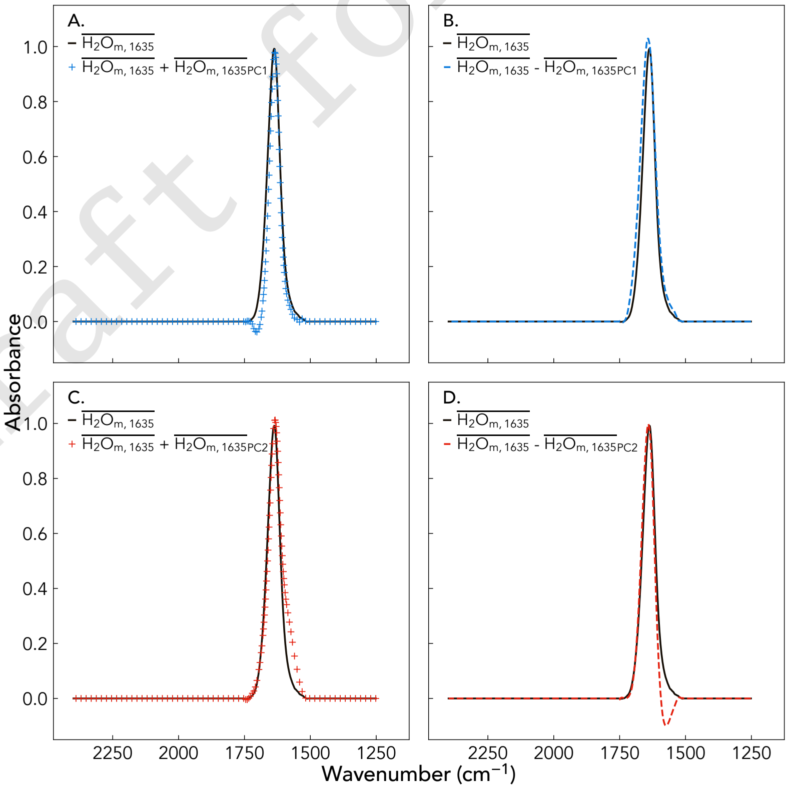

Figure 4: Mean $H_2O_{m,1635}$ peak ($\overline{H_2O_{m,1635}}$) with $\overline{H_2O_{m,1635}}_{PC1-2}$ describing variability in the nominal peak location. A. $\overline{H_2O_{m,1635}}$ + $\overline{H_2O_{m,1635}}_{PC1}$. B. $\overline{H_2O_{m,1635}}$ - $\overline{H_2O_{m,1635}}_{PC1}$. C. $\overline{H_2O_{m,1635}}$ + $\overline{H_2O_{m,1635}}_{PC2}$. D. $\overline{H_2O_{m,1635}}$ - $\overline{H_2O_{m,1635}}_{PC2}$.

considered the range of τ = 0.746-0.800, spanning silicic compositions from rhyolitic to albitic glasses. More experiments are needed to properly quantify the species-dependent nature of the $H_2O_{t,3550}$ peak. We find a positive relationship between $\varepsilon H_2O_{t,3550}$ and τ, despite complications presented by speciation. While endmember ε data for $H_2O_{t,3550}$ peak remain limited, $\varepsilon H_2O_{t,3550}$ is best described by τ (Figure 5). We do not observe a strong relationship in the full dataset between ε and NBO/T, calculated by the method outlined in Mysen and Richet [2018].

Dixon and Pan [1995] first demonstrated the dependence of ε for the CO_3^{2-} doublet molar absorptivities on η. The proportion of Na^+ to Ca^{2+} modulates the dissolution of C as molecular CO_2 and/or CO_3^{2-}. As the proportion of Ca^{2+} increases, εCO_3^{2-} decreases (Figure 5). Carbon dissolves as both molecular CO_2 and CO_3^{2-} in NaAl-rich silicate glasses (albitic, jadeitic, nephelinitic compositions) [Mysen and Virgo 1980a; b; Fine and Stolper 1985; Dixon and Pan 1995]. C dissolves solely as CO_3^{2-} in Ca and CaMg-rich silicate glasses (diopsidic, sodamelilitic, and akermanitic compositions) [Fine and Stolper 1986; Dixon and Pan 1995]. εCO_3^{2-} data are often limited to either the $\varepsilon CO^{2-}_{3,1515}$ or $\varepsilon CO^{2-}_{3,1430}$ peak, which are also assumed to be approximately equal [Dixon and Pan 1995]. We calculate a combined εCO_3^{2-} with data from $\varepsilon CO^{2-}_{3,1515}$ and $\varepsilon CO^{2-}_{3,1430}$, where available.

Uncertainties exist within both the compositional parameter and the quantification of ε. Higher uncertainties in compositional parameters may exist in older experimental studies where electron microprobe measurements quantified a limited number of oxide components. Variability in ε can also be attributed to variability in the baseline fitting method. $H_2O_{m,5200}$ and εOH^-_{4500} have been quantified with both linear and Gaussian baselines, resulting in differences in the determined ε. In order to account for uncertainties in a new regression of ε versus compositional parameters, we apply a variant of the inversion described in Chapter 9 of Menke [2018], with the implicit model:

$$f(x) = -\varepsilon + m_0 + m_1 p = 0, \tag{7}$$

where m is the vector of coefficients to be solved, p is the compositional parameter of interest, and x is the vector containing ε, compositional parameters, and vector of coefficients. The inversion applies Newton's method for determining the minimum of a function in a non-linear inverse problem. The Newtonian inversion derives strength from the ability to incorporate experimental and compositional uncertainties into the calibration and to utilize information on the shape of the error for a trial solution to successively derive improved fits for model parameters which minimize error. The full development and application of the implicit inversion technique is given in the Supplement, and the inversion code is available in the PyIRoGlass GitHub repository (github.com/sarahshi/PyIRoGlass).

We derive best-fit parameters and covariance matrices, evolving from the initial least squares fit to reach a minimum on the error surface, and compare these parameters against those from previous work (Figure 5). The problem is sufficiently overdetermined such that the solution does not depend significantly on the starting model and converges within 10 iterations. Best-fit compositional parameter multipliers (m_1) increase and intercepts (m_0) decrease for $\varepsilon H_2O_{m,5200}$, εOH^-_{4500}, and $\varepsilon H_2O_{m,1635}$ from the previous parameterizations of Mandeville et al. [2002]. Conversely, the best-fit compositional parameter decreases and the intercept increases for εCO_3^{2-} from the parameterization of Dixon and Pan [1995]. No previous calibrations of $\varepsilon H_2O_{t,3550}$ exist. Variance within calibrated ε differs significantly from the low variance $\varepsilon H_2O_{m,5200}$ and $\varepsilon H_2O_{m,1635}$ to high variance $\varepsilon H_2O_{t,3550}$. The $\varepsilon H_2O_{m,5200}$ covariance matrix is small given low variance within the data. The $\varepsilon H_2O_{m,1635}$ covariance matrix is similarly small given few calibration data. The εOH^-_{4500} covariance is slightly larger given higher variance within the data. $\varepsilon H_2O_{m,3550}$ variance is greater due to the increased variability in speciation due to quench temperatures and quench rates. εCO_3^{2-} variance is greater, particularly within the $\varepsilon CO^{2-}_{3,1515}$ calibrations, likely given convolution of the $H_2O_{m,1635}$ and the $CO^{2-}_{3,1515}$ tails.

Two forms of error—the error of calibration and the error of a single application of the inversion to the molar absorptivity—can be quantified. We define the error of calibration as being equal to the posterior covariance in ε, between the predicted and experimental ε. The 68% confidence interval of a single application of the model incorporates the calibration uncertainty as well as the analytical uncertainty of the calculated compositional parameter, applied with:

$$c_T = Z^T c_m Z + m^T c_z m, \tag{8}$$

where Z is a horizontal matrix of the measured compositional parameter, c_m is the diagonal posterior covariance on the model parameter coefficients, m is the horizontal matrix of the posterior model parameter coefficients, and c_z is a diagonal matrix of the uncertainty of measured compositional parameters. We are thus able to derive ε with a 68% confidence interval to account for both model and analytical uncertainty in a marked improvement to previous calibrations, where there are no estimates of the uncertainty of calibration. Application of the inversion with Equation 8 to the mid-ocean ridge basalt (MORB) composition of Dixon et al. [1995] predicts $\varepsilon H_2O_{m,5200}$ = 0.612±0.282, εOH^-_{4500} = 0.561±0.262, $\varepsilon H_2O_{m,1635}$ = 26.762±8.121, and $\varepsilon H_2O_{t,3550}$ = 60.046±7.075 L/mol·cm. Application of the inversion to the Etna alkali basalt of Shishkina et al. [2014] predicts εCO_3^{2-} = 303.918±16.626 L/mol·cm. Uncertainties associated with individual applications of the inversion are larger than those cited within the original study, but more accurately capture the uncertainty of regression.

2.3 Calculating Thickness and Density

We develop an automated implementation for calculating thicknesses from reflectance spectra by the interference fringe method. Interference fringes are produced by the interactions between reflected light and reflections internal to the sample, with fringe wavelengths inversely proportional to thickness and proportional to refractive index of the sample [Nishikida et al. 1996; Tamic et al. 2001; Wysoczanski and Tani 2006; Sun

Table 1: ε calibration data for H_2O and CO_2 species. τ and η values recalculated from reported compositions. Additional information regarding calibration uncertainties can be found in the PyIRoGlass GitHub repository.

Reference	Glass Composition	Analytical Method	τ	$\varepsilon H_2O_{m,5200}$ (L/mol·cm)	εOH^-_{4500} (L/mol·cm)	$\varepsilon H_2O_{m,3550}$ (L/mol·cm)	$\varepsilon H_2O_{m,1635}$ (L/mol·cm)
Shishkina et al. [2014]	Nephelinite, E2624	KFT, EA	0.508			56.7	
Shishkina et al. [2014]	Basanite, A2549	KFT, EA	0.532			57.3	
Shishkina et al. [2014]	Alkali basalt, B2518	KFT, EA	0.585			60.3	
Shishkina et al. [2014]	Alkali basalt, B2507	KFT, EA	0.585			60.5	
Mercier et al. [2010]	Basanite	KFT	0.588			43.96	
Acocella et al. [1984]	$NA_2O*3SiO_2$	Experimental Loading	0.600	0.634	0.267		
Lesne et al. [2011]	Basalt (Vesuvius)	KFT	0.607	0.57	0.7		
Behrens et al. [2009]	Ultrapotassic melt	KFT, EA	0.622	1.02	0.62	63.9	
Dixon et al. [1995]	MORB	Manometry	0.627	0.62	0.67	63	25
Ohlhorst et al. [2001]	Basalt	KFT	0.629	0.66	0.57		
Lesne et al. [2011]	Basalt (Stromboli)	KFT	0.630	0.62	0.97		
Lesne et al. [2011]	Basalt (Etna)	KFT	0.631	0.56	0.75		
Stolper [1982]	Basalt SLNT	Manometry	0.636			64	
Stolper [1982]	Basalt Bouvet CHN	Manometry	0.639			72	
Pandya et al. [1992]	Basalt	Mass Spectrometry	0.643			61	
Jendrzejewski et al. [1997]	MORB	Manometry	0.645			78	
Vetere et al. [2011]	Shoshonite	KFT	0.659	1.03	0.8		
Di Matteo et al. [2006]	Shoshonite	KFT	0.663			60	
Shishkina et al. [2010]	Basalt	KFT, EA	0.664	0.65	0.69	65	
Shishkina et al. [2010]	Basalt	KFT, EA	0.664	0.65	0.69	65	
Yamashita et al. [1997]	Tholeiite	Manometry	0.665	0.84	0.85	64	
Mercier et al. [2010]	Basalt	KFT	0.666			62.8	
Stolper [1982]	Basalt Marianas 46D-I-1	Manometry	0.668			67	
Yamashita et al. [1997]	High Al Basalt	Manometry	0.671	0.84	0.85	64	
Fiege et al. [2015]	Mg-poor basalt	KFT	0.689	0.848	1.161		
Stolper [1982]	Basalt Tasaday	Manometry	0.691			75	
Jakobsson [1997]	Icelandite	EA	0.708	1.25	0.95		42
Di Matteo et al. [2006]	Latite	KFT	0.712			60	
Carroll and Blank [1997]	Phonolite	Manometry	0.720	1.10	1.25		
Ohlhorst et al. [2001]	Andesite	KFT	0.722	0.90	0.77		
King et al. [2002]	Andesite	Manometry, SIMS	0.743	1.08	1.15	70.3	40.8
Mandeville et al. [2002]	Fe-Bearing Andesite	Manometry	0.746	1.07	0.79	62.32	42.34
Di Matteo et al. [2004]	Trachyte	KFT	0.755	1.36	1.58		
Vetere et al. [2006]	Fe-Free Andesite	KFT	0.756	1.04	0.92		
Silver et al. [1990]	Jadeite Glass	Manometry	0.756	1.13	1.12		
Silver et al. [1990]	CAS-E2	Manometry	0.774	1.07	0.85		
Yamashita et al. [1997]	Dacite	Manometry	0.782	1.60	0.94	68	
Ohlhorst et al. [2001]	Dacite	KFT	0.783	1.17	1.02		
Allabar and Nowak [2020]	Peralkaline rhyolite	KFT	0.791	1.20	1.5		
Mandeville et al. [2002]	Fe-Free Andesite	Manometry	0.795	1.46	0.89	69.21	52.05
Withers and Behrens [1999]	Albite, 300 K	KFT	0.797	1.47	1.27		
Silver et al. [1990]	Orthoclase, KAS	Manometry	0.799	1.87	1.43		
Behrens [1995]	Albite	KFT	0.799	1.49	1.28		
Silver and Stolper [1989]	Albite	Manometry, NMR	0.799	1.67	1.13	70	49
Behrens et al. [1996]	Orthoclase, K100	KFT	0.806	1.65	1.58		
Stolper [1982]	Hydrated Obsidian OBS G	Manometry	0.811			55	
Stolper [1982]	Hydrated Obsidian OBS I	Manometry	0.813			66	
Stolper [1982]	Hydrated Obsidian OBS E	Manometry	0.813			73	
Nowak and Behrens [1995]	Haplogranite	KFT	0.850	1.79	1.56		
Stabile et al. [2020]	Pantellerite	KFT	0.853	1.97	0.99		
Leschik et al. [2004]	Rhyolite	KFT	0.856			80	
Withers and Behrens [1999]	Rhyolite	KFT	0.856	1.69	1.47		
Newman et al. [1986]	Rhyolite	Manometry	0.859	1.61	1.73	100	55
Hauri et al. [2002]	Rhyolite	SIMS	0.859			90	56
Okumura and Nakashima [2005]	Rhyolite	KFT	0.860	1.75	1.42		
Ihinger et al. [1994]	Rhyolite	Manometry	0.860	1.86	1.5	80	55
Aubaud et al. [2009]	Rhyolite	ERDA	0.860			95	
Okumura et al. [2003]	Rhyolite	KFT	0.864			75	
Silver et al. [1990]	Rhyolite	Manometry	0.864	1.61	1.73		
Dobson et al. [1989]	Rhyolite	Manometry	0.867			88	
Stolper [1982]	Synthetic Albite A78-56	Manometry	0.902			88	

Reference	Glass Composition	Analytical Method	η	$\varepsilon CO^{2-}_{3,1515}$ (L/mol·cm)	$\sigma\varepsilon CO^{2-}_{3,1515}$ (L/mol·cm)	$\varepsilon CO^{2-}_{3,1430}$ (L/mol·cm)	$\sigma\varepsilon CO^{2-}_{3,1430}$ (L/mol·cm)
Behrens et al. [2009]	Ultrapotassic	KFT, EA	0.2316	308	110		
Vetere et al. [2014]	Phonotephrite AH1	KFT, EA	0.2369			294	16
Jendrzejewski et al. [1997]	MORB	Manometry	0.2446	398	10	398	10
Brounce et al. [2021]	Boninite	EA	0.2630			265	30
Dixon and Pan [1995]	Basanite	EA	0.2680	284	5	281	6
Fine and Stolper [1986]	Basalt	NRA	0.2680	375	20	375	20
Shishkina et al. [2014]	MORB, 169oxi	KFT, EA	0.2755	359	25	306	11
Shishkina et al. [2010]	Basalt	KFT, EA	0.2766	361	43	317	23
Thibault and Holloway [1994]	Leucitite	SIMS	0.2883	355		355	
Shishkina et al. [2014]	Ferro-basalt, SC1	KFT, EA	0.3028	372	14	329	15
Shishkina et al. [2014]	Basanite, A2549	KFT, EA	0.3610	349	25	306	32
Shishkina et al. [2014]	Alkali basalt, OB93	KFT, EA	0.3669	385	18	341	19
Shishkina et al. [2014]	Alkali basalt, Etna	KFT, EA	0.3670	394	27	360	24
Shishkina et al. [2014]	Alkali basalt, B2507	KFT, EA	0.3912	380	30	311	41
Vetere et al. [2014]	Phonotephrite AH2	KFT, EA	0.4241			244	15
Vetere et al. [2011]	Shoshonite	KFT, EA	0.4384			356	18
Jakobsson [1997]	Icelandite	EA	0.5074	180	15	190	15
Vetere et al. [2014]	Phonotephrite AH3	KFT, EA	0.5369			264	15
Vetere et al. [2014]	Latite	KFT, EA	0.5903			215	8
Duncan and Dasgupta [2015]	Rhyolite	SIMS	0.8406	207	22	143	10

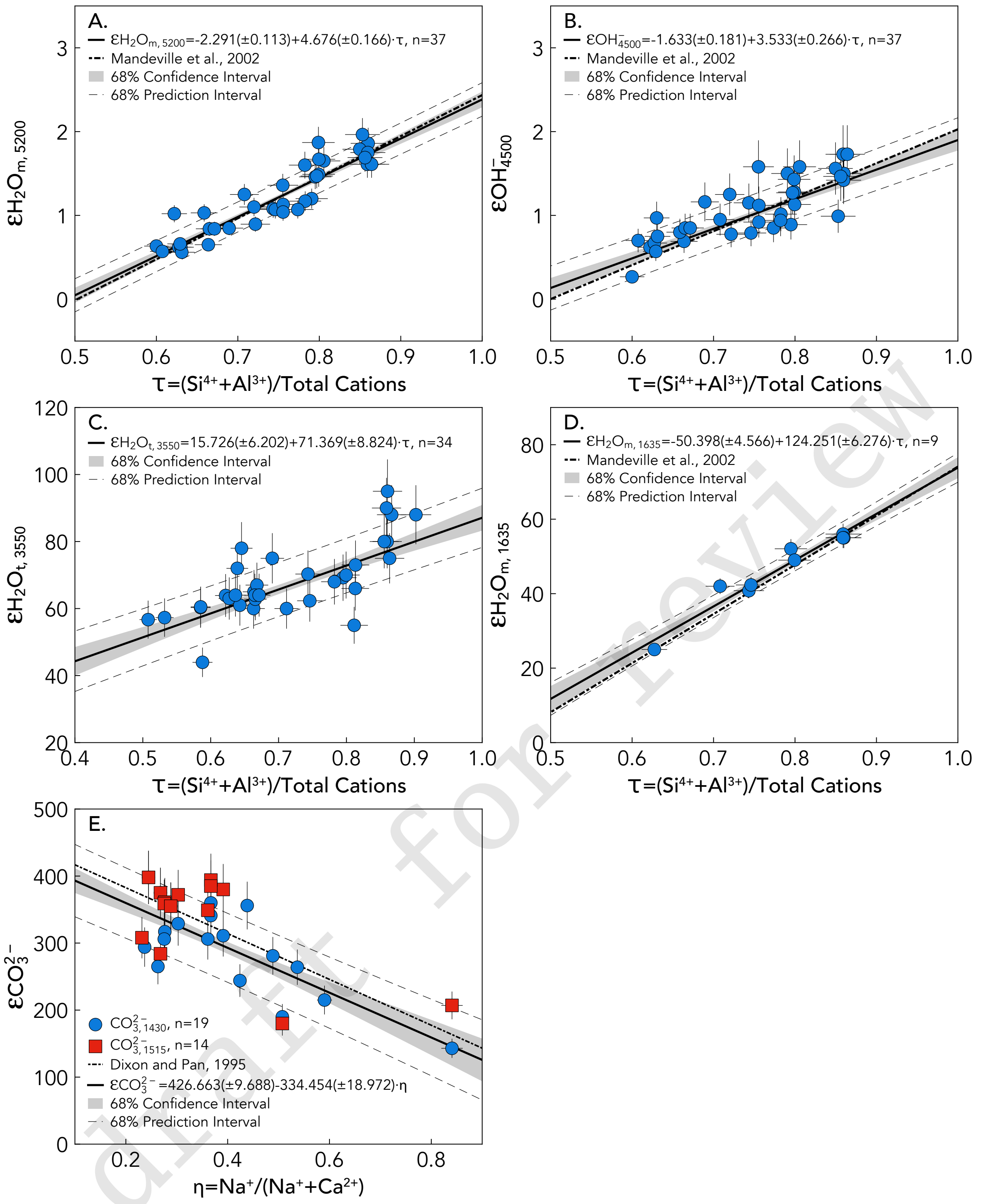

Figure 5: Tetrahedral cation fraction τ = (Si^{4+}+Al^{3+})/(total cations) against: A. $\varepsilon H_2O_{m,5200}$. B. εOH^-_{4500}. C. $\varepsilon H_2O_{t,3550}$. D. $\varepsilon H_2O_{m,1635}$. E. Cation fraction η= Na$^+$/(Na$^+$+Ca^{2+}) against εCO_3^{2-}.

et al. 2007]. Interference fringes from the reflectance spectra of two olivine samples are shown in Figure 6. Nishikida et al. [1996] show the relationship applicable to glasses and olivine:

$$l = \frac{m}{2n(v_1 - v_2)} \tag{9}$$

where l is the thickness of area analyzed, m is the number of fringes in the wavenumber range, n is the refractive index of the material, and v_1 and v_2 are the highest and lowest wavenumbers in the interval.

Signal-to-noise ratios associated with interference fringes in reflectance spectra can be low. Reflectance spectra are pre-processed with median filtering to remove potential single spike noise and successively processed with Savitzky-Golay filtering, fitting low-degree polynomials to data with linear least squares, shown in Figure 6 [Savitzky and Golay 1964]. Savitzky-Golay filtering improves signal quality by removing additional noise, but impacts peak amplitudes variably. Sinusoidal peaks with smooth extrema are not strongly impacted by filtering (Figure 6A), but peaks with sharp extrema are reduced in amplitude (Figure 6B). The locations of the peaks in filtered spectra do not differ significantly despite the difference in amplitude. Local extrema associated with each interference fringe wave are located by identifying regions of greatest absorbance change. Maxima are surrounded by points that are lower in absorbance and minima are surrounded by points that are greater in absorbance. Individual local extrema identification by differentiation can fail with noisier spectra, but consideration of all peaks within the wavenumber range allows for uncertainty assessment. Thicknesses are calculated from the wavenumber differences (λ) between all adjacent local extrema in the specified wavenumber range. Uncertainties in thickness are calculated from the standard deviation of all local maxima and minima-derived thicknesses. Individual thicknesses falling outside one standard deviation of the mean are removed.

The mean and standard deviation of thicknesses from interference fringes were compared against those determined using a Mitutoyo 543-783B Digimatic Indicator for Volcán de Fuego olivines in the wavenumber range of 2800 to 2000 cm^{-1}, to assess the uncertainty associated with this automated method. A refractive index of 1.709 was determined using the orientation- and forsterite-dependent parameterization of olivine refractive index from Howie et al. [1992] with a forsterite content of 72 (the mean composition measured next to the studied melt inclusions). Mean thicknesses calculated from interference fringes compare well with those from digital micrometer measurements (Figure 7). Agreement within thicknesses is demonstrated by the high concordance correlation coefficient (CCC, a measurement of the agreement between two variables [Lin 1989]), low root-mean-square error (RMSE), low relative root-mean-square error (RRMSE), high coefficient of determination (R^2), slope (m) nearing 1, and intercept (b) nearing 0. Mean thickness uncertainties from five repeat measurements are similar to previously reported values of less than 3 μm [Nichols and Wysoczanski 2007; von Aulock et al. 2014; Allison et al. 2019].

Melt density is a function of glass composition and is calculated from the gram formula weight and partial molar volumes from Lesher and Spera [2015], at ambient temperature and pressure of the analytical conditions at 25°C and 1 bar. The large molar volume of H_2O significantly impacts density and requires the implementation of an iterative solver. Density is initially assumed to have no contribution from H_2O but is iteratively updated with the calculated amount of $H_2O_{t,3550}$ or $H_2O_{m,1635}$ + OH^-_{4500} if the sample is saturated (see Section 3.4). The density calculation is repeated to ensure stability; it generally converges within 10 iterations.

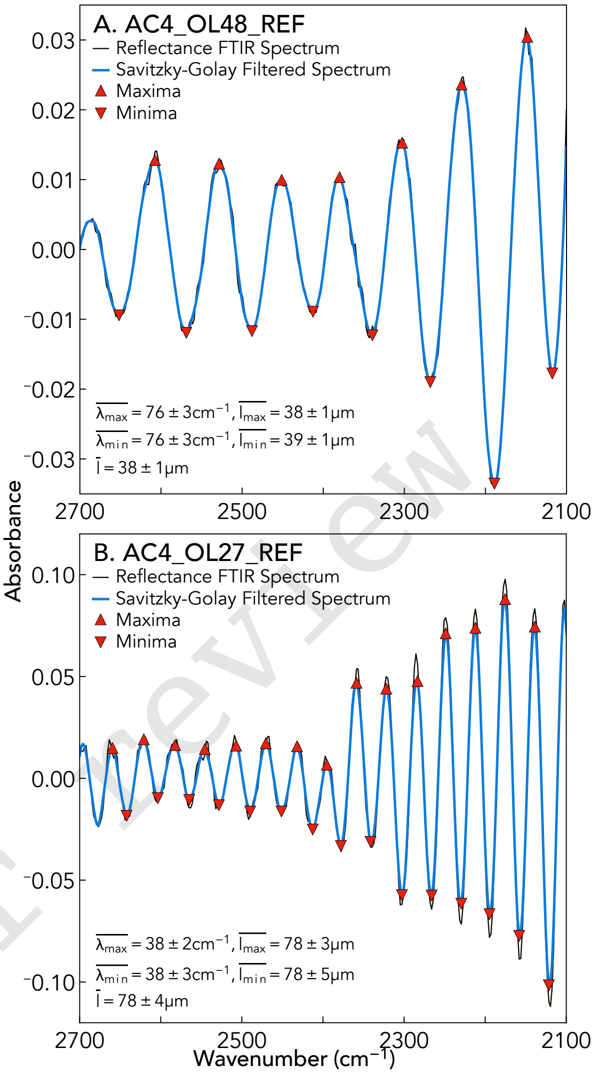

Figure 6: Reflectance FTIR spectra with interference fringes for olivines from Volcán de Fuego, Guatemala. The relationship between wavenumber differences (λ) and wafer thickness is negative, as larger differences are associated with lower thicknesses. A. Olivine wafer VF18-AC4-OL48 (black) with Savitzky-Golay smoothed spectrum (blue) and identified extrema (red triangles). OL48 spectrum and filtered spectrum are sinusoidal and smooth, with strong agreement between the raw and smoothed spectra. B. Olivine wafer VF18-AC4-OL27 with initially sharp, singular peaks; Savitzky-Golay smoothed spectrum has reduced amplitudes. Local extrema wavenumbers locations remain well reproduced. Local extrema are more closely spaced than those from OL48, thus OL27 is thinner.

2.4 PyIRoGlass: An MCMC Algorithm for Calculating Volatile Concentrations with Uncertainties

The net equation describing the absorbance spectrum of a glass or melt inclusion, with υ^- defined as the wavenumber range from 2400 to 1250 cm^{-1}, is expressed in the following form:

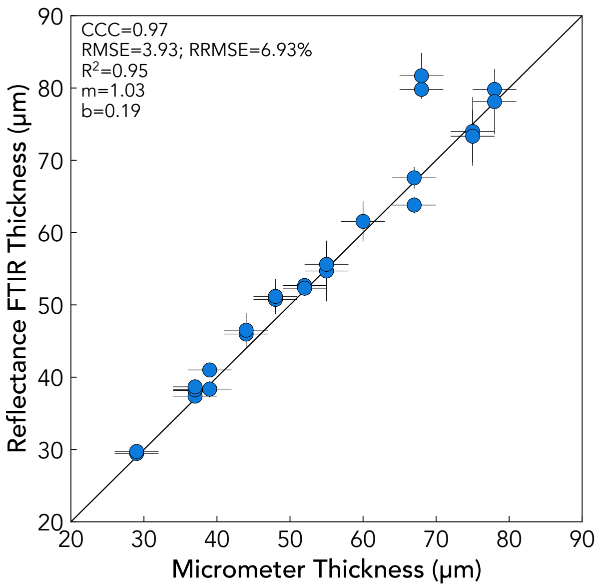

Figure 7: Thicknesses from interference fringes of FTIR spectra compared to those from digital micrometer. Uncertainties on interference fringe thicknesses are calculated from the standard deviation of all maxima- and minima-related thicknesses within the wavenumber range of 2800 to 2000 cm^{-1}. Uncertainties on thicknesses from the digital micrometer are set at the stated uncertainty of 3 μm. Agreement between calculated and measured thicknesses is indicated by high CCC, low RMSE (μm unit) and RRMSE (unitless), high R^2, m nearing 1, and b nearing 0.

$$\begin{aligned}\hat{A} = \quad & x_0\overline{B} + x_1\overline{B}_{PC1} + x_2\overline{B}_{PC2} + x_3\overline{B}_{PC3} + x_4\overline{B}_{PC4} \\ & + y_0\overline{H_2O_{m,1635}} + y_1\overline{H_2O_{m,1635}}_{PC1} + y_2\overline{H_2O_{m,1635}}_{PC2} \\ & + \frac{a_{1515}}{2\sigma_{1515}^2} \cdot e^{-(\upsilon^{-}-\mu_{1515})^2} + \frac{a_{1430}}{2\sigma_{1430}^2} \cdot e^{-(\upsilon^{-}-\mu_{1430})^2} \\ & + m\upsilon + b\end{aligned} \tag{10}$$

where x_0, x_1, x_2, x_3, x_4, y_0, y_1, y_2, a_{1515}, a_{1430}, σ_{1515}, σ_{1430}, μ_{1515}, μ_{1430}, m, and b are the best-fit coefficients or parameters. x_n and y_n respectively describe best-fit coefficients for the mean baseline or peak and the principal components associated with the baseline or peak. The remaining variables describe best-fit parameters.

These best-fit coefficients or parameters are first initialized with ordinary least squares. The parameter space of the modeled absorbance of the transmission FTIR spectrum is sampled and explored by leveraging a Markov Chain Monte Carlo sampler in a Bayesian parametric framework, to account for uncertainty. In this framework of Bayesian inference, the posterior joint probability distribution of model parameters is quantified as a function of the prior probability of model parameters and a likelihood function. Bayes' Theorem dictates that the posterior joint probability distribution is updated as more information becomes available, following Cubillos et al. [2017]:

Table 2: PyIRoGlass parameters and coefficients fitting Equation 10.

Abbreviation	Coefficient or Parameter
$\overline{B}$	Mean degassed baseline
$\overline{B}_{PCn}$	n-th principal component of baseline
x_n	Best-fit coefficient for baseline-related terms
$\overline{H_2O_{m,1635}}$	Mean $H_2O_{m,1635}$ peak
$\overline{H_2O_{m,1635}}_{PCn}$	n-th principal component of $H_2O_{m,1635}$ peak
y_n	Best-fit coefficient for $H_2O_{m,1635}$-related terms
$a_{1515/1430}$	CO_3^{2-} peak amplitude
$\mu_{1515/1430}$	CO_3^{2-} peak center
$\sigma_{1515/1430}$	CO_3^{2-} peak half-width
υ^{-}	Wavenumber fitting range
m	Slope of linear tilt
b	Intercept of linear tilt

$$P(\theta|y, M) \propto P(\theta|M)P(y|\theta, M), \tag{11}$$

where y denotes data, θ is the set of parameters, $P(\theta|y, M)$ is the posterior probability distribution of parameters, $P(\theta|M)$ is the prior probability distribution (not incorporating new information), and $P(y|\theta, M)$ is the likelihood. The prior probability distribution of parameters is defined by the expected range and distributions of these parameters. The likelihood serves as the probability density function of the modeled data, given an array of parameters. A Markov Chain Monte Carlo (MCMC) algorithm was utilized to generate random samples from the parameter space that hold a probability density distribution that is proportional to the posterior probability distribution. The MCMC approach utilizes a series of jumps between samples, to effectively traverse and explore parameter space. The open-source Python package, Multi-Core Markov Chain Monte Carlo (mc^3), developed by Cubillos et al. [2017] integrates these statistical methods and was implemented for this study.

Fixed absorbance spectra provide the information required to refine posterior probability distributions of model parameters. Prior probability distributions describing the baseline, peaks, and lines can be characterized using either uniform or Gaussian distributions. Uniform priors assign equal probabilities across their defined range, making all values equally probable. In contrast, Gaussian priors assign probabilities based on a Gaussian probability distribution, characterized by its mean and standard deviation. Parameters related to the baseline, H_2O_m peak, CO_3^{2-} doublet peak heights, and linear adjustment are sampled uniformly due to the larger variability in these parameters in the absence of *a priori* knowledge. The exploration space of these uniformly sampled priors is informed by the initial model generation process. The CO_3^{2-} doublet peak locations and half-widths are defined with Gaussian priors, reflecting the well-established nature of these parameters in the absorbance spectra of basaltic to andesitic glasses. The initial parameters for these priors are optimized with the least squares Trust Region Reflective algorithm, which is particularly suited for well-constrained, large problems [Branch et al. 1999].

We implement PyIRoGlass using 10^6 samples, 9 chains, and $2 \cdot 10^4$ burn-in samples. We employ the Snooker Updater Differential Evolution Markov Chain method (DEMC) for random MCMC sampling [ter Braak 2006; ter Braak and Vrugt 2008]. In the Snooker Updater DEMC algorithm, N chains are computed in parallel. The algorithm computes the differences between the chain from which the jump is being proposed and the remaining chains ($N - 1$), utilizing the differences to determine the scale and orientation of each proposed jump [ter Braak and Vrugt 2008]. The chains converge towards a posterior distribution, ensuring that evolution is oriented correctly and scaled appropriately. We apply a Gelman-Rubin convergence criterion with a threshold of 1.01 to assess convergence. The Gelman-Rubin convergence criterion determines differences both within and across chains. When the variance between chains is minimal, the Gelman-Rubin convergence criterion should approach 1, indicating that the chains have effectively converged to the posterior distribution [Gelman and Rubin 1992]. The MCMC will thus terminate early. The Snooker Updater DEMC optimizes acceptance rates and efficiency. Processing a single transmission spectrum and generating plotting files takes approximately 1 minute on a Macbook Pro with a 2.6 GHz 6-Core Intel Core i7. The same task takes about 2 minutes on the cloud-based Python development environment of Google Colab.

PyIRoGlass calculates volatile concentrations with their associated uncertainties using a final MCMC scheme with all parameters in the Beer-Lambert Law. ALS (Section *2.1.1*) and mc^3 baseline-derived peak heights (Section *2.1.2*) are used to determine concentrations of H_2O_t, H_2O_m, OH^-, and CO_2, with glass composition used to determine the composition-dependent ε (Section 2.2) and to iteratively determine density (Section 2.3), all as a function of sample thickness (Section 2.3). The best-fit peak heights, molar absorptivities, thicknesses, and densities are applied in the Beer-Lambert Law to determine the concentration of each peak. A standard deviation on each concentration is taken by running a simple Monte Carlo error assessment in which all parameters, except molar mass, are allowed to vary with Gaussian distributions for $5 \text{x} 10^5$ samples.

3 APPLICATION AND VALIDATION OF PYIROGLASS

3.1 PyIRoGlass Structure and Packaging

3.1.1 *Installation*

PyIRoGlass can be locally installed with with Python versions 3.7-3.11 through the command line:

```
pip install PyIRoGlass
```

We further provide a cloud-based Python development environment in Google Colab, with links provided on the PyIRoGlass GitHub repository. These implementations create interactive computing environments without the necessity for locally installing Python. In these cloud-based Python development environments, installation instead occurs within a code cell:

```
!pip install PyIRoGlass
```

Following installation, the PyIRoGlass package must then be imported and initialized with:

```
import PyIRoGlass as pig
```

Functions from PyIRoGlass are then called with the abbreviated package name, followed by the function name. The primary functions required for processing transmission FTIR spectra with PyIRoGlass include the function loading all spectra, function loading chemistry and thickness information, and the function processing all spectra. The function loading transmission FTIR spectrum files is called as follows:

```
pig.Load_SampleCSV(args)
```

and identifies all spectrum files within a directory. The function loading the chemistry and thickness file is called as follows:

```
pig.Load_ChemistryThickness(args)
```

The function then processing each spectrum file is called as follows:

```
pig.Run_All_Spectra(args)
```

All functions require the input of specific variables within the parentheses, called arguments (abbreviated to args).

The additional functions for processing reflectance FTIR spectra with FTIR include the function loading spectra and the function for identifying peaks and determining thicknesses. The same function is used for loading reflectance FTIR spectra, as for loading transmission FTIR spectra. The function determining all thicknesses is called as follows:

```
pig.Thickness_Process(args)
```

All available functions and arguments required can be accessed and explored in the PyIRoGlass Read the Docs (pyiroglass.readthedocs.io). The cloud-based Python development environments are recommended for ease of use for Python beginners, but significant computational gains are provided by running the code locally.

3.1.2 *Data Input*

The two required types of input files include the FTIR spectrum file and the chemistry and thickness file. Each FTIR spectrum is input as a CSV file, unmodified from the Thermo Scientific Nicolet iN10 MX Fourier Transform Infrared Spectrometer outputs, with a wavenumber and absorbance column. The chemistry and thickness file is structured as a CSV file with columns with headers: Sample, SiO_2, TiO_2, Al_2O_3, Fe_2O_3, FeO, MnO, MgO, CaO, Na_2O, K_2O, P_2O_5, Thickness, and Sigma_Thickness. Sample input files are provided in the PyIRoGlass GitHub repository.

3.1.3 *Code Input*

Computational workflow examples for PyIRoGlass are provided in the run file examples on the PyIRoGlass GitHub repository and Google Colab. The workflow is structured such that the sole modifications required are changes to the paths to input files, shown as follows:

```python
import os
import glob
path_spec = os.getcwd() + '/Inputs/TransmissionSpectra/'
path_chemthick = os.getcwd() + '/Inputs/ChemThick.csv'
spectra = sorted(glob.glob(path_spec + "*"))
output_path = os.getcwd() + '/Outputs/'
```

These lines of code are used to navigate to the paths of directories and files. In this case, we have a directory called PyIRoGlass with the primary code run file (where this code would be found) and a directory called Inputs. The Inputs directory contains a sub-directory of transmission FTIR spectra and a CSV of chemistry and thickness. The sub-directory is called TransmissionSpectra and contains the transmission FTIR spectra of interest, which can be batched and run at the same time. One additional file of chemistry and thickness for all the spectra of interest is called 'ChemThick.csv'. The following functions within PyIRoGlass are used to load and read these files as Python dataframes or dictionaries.

```python
COMP, THICKNESS = pig.Load_ChemistryThickness(
        path_chemthick)
DFS_FILES, DFS_DICT = pig.Load_SampleCSV(spectra, wn_high
        = 5500, wn_low = 1000)
```

The spectra can then be batch processed through PyBaselines with the saved outputs:

```python
DF_OUTPUT, FAILURES = pig.Run_All_Spectra(DFS_DICT,
        output_path)
DF_OUTPUT.to_csv(output_path + '_DF.csv')

T_ROOM = 25 # C
P_ROOM = 1 # Bar
N = 500000 # Concentration MCMC iterations
DENSITY_EPSILON, MEGA_SPREADSHEET = pig.
        Concentration_Output(DF_OUTPUT, N, THICKNESS, COMP
        , T_ROOM, P_ROOM)
DENSITY_EPSILON.to_csv(output_path + '_DensityEpsilon.csv')
MEGA_SPREADSHEET.to_csv(output_path + '_H2OCO2.csv')
```

The transmission FTIR spectra names and data dictionary and a list containing paths to the input files are input into the Run_All_Spectra function. All parameters—most importantly, peak heights with uncertainties—sampled from the ALS and mc^3 fitting of all species peaks are returned within the DF_OUTPUT dataframe. Concentrations are finally calculated with the Concentration_Output function, with the arguments of the dataframe of peak heights with uncertainties, number of samples for Monte Carlo error assessment, sample thickness, sample chemistry, and temperature and pressure of analysis. Concentration_Output returns two dataframes: DENSITY_EPSILON, which contains sample density and molar absorptivities with their uncertainties, and MEGA_SPREADSHEET, which provides volatile concentrations with uncertainties, information on peak saturation, and signal-to-noise ratios. Both dataframes are saved for future reference.

3.1.4 *Data and File Output*

PyIRoGlass returns five forms of outputs: dataframes including concentrations with uncertainties, peak heights, and densities and absorption coefficients; figures of peak fits, histograms of explored fit parameter space, pairwise plots of parameter space, and trace plots of explored parameter space; log (.log), text (.txt), and zipped (.npz) files recording explored parameter space and statistics. We will walk through one instance of PyIRoGlass and show the output files in Section 3.3. Additional examples of output files are provided in the PyIRoGlass GitHub repository.

3.1.5 *Unit Testing*

To ensure the reliability and robustness of the PyIRoGlass package for FTIR spectra processing, we implemented a comprehensive suite of unit tests. Unit tests are a foundational component of software engineering. The primary objective of unit tests is to validate that each function in the package works as expected and to detect potential regressions during development as new features are added, modifications are made, or package versions are updated. We develop unit tests for most functions within the code:

1. **Data Loading**: Ingest data to ensure consistent format for package integration.
2. **Fitting Functions**: Validate Markov Chain Monte Carlo outputs of VF18-AC4-OL49 and VF18-AC4-OL53 for peak height consistency up to the third decimal, permitting some variability within the sampling regime. Confirm ALS-derived peak heights for consistency up to the fifth decimal.
3. **Concentration, Density, Epsilon Calculations**: Cross-check algorithms against select samples for glass compositions and transmission FTIR spectra. Ensure that volatile concentrations agree up to the fifth decimal place and that Monte Carlo errors agree within 0.01 wt.% for H_2O and 1 ppm for CO_2.
4. **Thickness Calculations**: Assess the agreement in thicknesses derived from interference fringes of reflectance FTIR up to the fifth decimal, accounting for associated uncertainties.
5. **Plotting**: Implement tests to ensure plots are generated accurately and consistently.
6. **Inversions**: Examine Newtonian inversions for molar absorptivity to ensure correct determinations of fitting parameters and uncertainties to the fifth decimal.

We utilize the pytest package and framework for executing tests. The choice of pytest was motivated by its widespread adoption in the Python community, its rich ecosystem, and its flexibility in handling test scenarios. At each instance of modification to the package code, the unit tests are automatically executed within GitHub Workflows. This ensures that the performance and integrity of the software remains intact with every change. Our unit testing currently covers 94% of the PyIRoGlass's code. This provides a quantifiable metric of how much of the software's functionality is tested automatically for reproducibility. Through this extensive and tailored test suite, we aim to capture potential anomalies, inaccuracies, or failures in the spectrum processing pipeline, ensuring the PyIRoGlass's reliability across its breadth of functionalities.

3.2 Volcán de Fuego Melt Inclusions: A Test Dataset

We demonstrate the performance of PyIRoGlass with a test dataset of melt inclusions from the 2018 eruption of Volcán de Fuego, Guatemala. This excercise underscores the variable quality of output peak information. Samples consist of Aguas Calientes (AC4, IGSN: TAP000081) tephra fall deposits from the largest ash plume of the Volcán de Fuego eruption of June 3, 2018. These samples are the focus of a study currently underway [Shi et al. 2021]. Natural glass standards and olivine-hosted melt inclusions (MIs) were analyzed with the Thermo Scientific Nicolet iN10 MX Fourier Transform Infrared Spectrometer at the Lamont-Doherty Earth Observatory. Dry and CO_2-scrubbed air purged the machine and measurements were made on a liquid nitrogen-cooled MCT-A detector. Our methodology for preparing samples and analyzing melt inclusions by FTIR is further described in the Supplement. Periodic internal check standard analyses of back-arc basin glass D1010 and melt inclusions CN-C-OL1', CN92C-OL2, and ETF46 were performed through each analytical session, as in-house check standards. We found it to be good practice to measure these check standards regularly to ensure data quality.

3.3 Volcán de Fuego Melt Inclusions: Parameter Posteriors and Spectrum Fits

Posterior distributions from one application of PyIRoGlass informs our understanding of the relationships between parameters and their underlying uncertainties. Figure 8 shows the parameter posterior probability density distributions, when applied to melt inclusion VF18-AC4-OL49. Strong correlations exist between the posterior probabilities of the best-fit baseline-generating coefficients of x_0 scaling $\overline{B}$, x_1 scaling $\overline{B}_{PC1}$, x_2 scaling $\overline{B}_{PC2}$, x_3 scaling $\overline{B}_{PC3}$, x_4 scaling $\overline{B}_{PC4}$, m, and b. This suggests that there is non-uniqueness in the sampled best-fit solutions, resulting in a strong positive covariance structure between x_0, x_1, and x_3, as well as a negative covariance structure between x_0, x_2, and x_4. The posterior probabilities of m and b are strongly negatively correlated, which further highlights the non-unique balance between parameters.

The posterior probabilities of the parameters fitting the CO_3^{2-} doublet reveal positive correlations in the peak-amplitude related a_{1515} and a_{1430} parameters. This indicates that the CO_3^{2-} doublet peaks should possess similar amplitudes, consistent with the assumptions of Dixon and Pan [1995]. The parameters y_0, y_1, and y_2, which fit the $H_2O_{m,1635}$ peak are correlated with the parameters fitting the $CO^{2-}_{3,1515}$ peak, which is expected given the proximity of the peaks and potential convolution of the tails. However, the peak amplitude modulating parameter ($\overline{H_2O_{m,1635}}$) shows no correlation with the parameters fitting the $CO^{2-}_{3,1515}$ peak. The peak position modulating parameters, y_1 and y_2, respectively show positive and negative correlations with σ_{1515}, the parameter controlling the half-width of the $CO^{2-}_{3,1515}$ peak. These findings underscore the importance of accounting for covariance between parameters in ensemble Bayesian frameworks when fitting baselines and peaks to FTIR spectra, especially for accurately assessing volatile concentration uncertainties.

Figure 9 shows the resulting baseline and peak fits from PyIRoGlass for melt inclusion VF18-AC4-OL49, which is also the subject of Figure 1 and of the unit testing described in Section *3.1.5*. The melt inclusion is saturated in $H_2O_{t,3550}$, given the ragged peak and absorbance exceeding 2, resulting in the need to combine H_2O_m and OH^-_{4500} to quantify H_2O_t (Figure 9A). We sample the uncertainty in near-infrared peak height by fitting three ALS baselines with variable wavenumber fitting ranges to the $H_2O_{m,5200}$ and OH^-_{4500} peaks (Figure 9B). The baseline-subtracted $H_2O_{m,5200}$ and OH^-_{4500} peaks are then interpolated with kriging to reduce noise within the peaks (Figure 9C), and quantify the maximum peak height [Krige 1951; Cressie 1990]. Variability within the smoothed peak heights is observed, given the uncertainty in some of the fitting ranges for these peaks. Both near-infrared peaks have signal-to-noise ratios exceeding 4, representing meaningful signals. The $H_2O_{t,3550}$ peak is similarly fit with three ALS baselines and median filtered to reduce single spike noise (Figure 9D). The peak is not used in this sample given saturation and the introduction of non-linearity to the Beer-Lambert Law. Baseline and peaks, fit simultaneously, for the $H_2O_{m,1635}$ peak and CO_3^{2-} doublet are generated and sampled through 10^6 iterations (Figure 9E). The peak heights and concentrations for both peaks in the CO_3^{2-} doublet are near identical. We report CO_2 as the mean of the CO_3^{2-} doublet peaks. The PyIRoGlass fit to this transmission FTIR spectrum sees residuals in absorbance of less than 0.01 in the region of interest beneath the $H_2O_{m,1635}$ peak and CO_3^{2-} doublet. The combination of the Bayesian framework and fitting technique allows for robust determinations of both volatile concentrations and their uncertainties.

3.4 Observations on H_2O Species Peak Quality

The derivation of concentrations from the $H_2O_{m,1635}$ and $H_2O_{m,5200}$ peaks prompts the question of their relative quality and performance. We determine H_2O species concentrations with PyIRoGlass to compare the H_2O_m peaks in the test dataset of Volcán de Fuego melt inclusions and the internal check standards noted above (Figure 10). The Volcán de Fuego melt inclusions form the primary basis of this analysis, given the compositional heterogeneity and matrix-matching of the samples. Repeated measurements of the internal check standards allows for assessment of variability in the $H_2O_{m,1635}$ and $H_2O_{m,5200}$ peaks through time. Triplicate analyses of internal check standards were made through each of the 12 analytical sessions, periodically spaced through the session. Both datasets are filtered to only contain analyses where near-infrared peaks have signal-to-noise ratios exceeding 4.

$H_2O_{m,5200}$ primarily predicts concentrations greater than those from $H_2O_{m,1635}$ in the Volcán de Fuego melt inclusions (Figure 10A) and internal check standards (Figure 10B, see Section 3.5 and Table 4). Most analyses fall above the 1-1 line and the slopes fit to the datasets exceed 1. Two clusters of internal check standards—back-arc basin glass D1010 ($H_2O_{m,1635}$~0.15 wt.%) and Cerro Negro melt inclu-

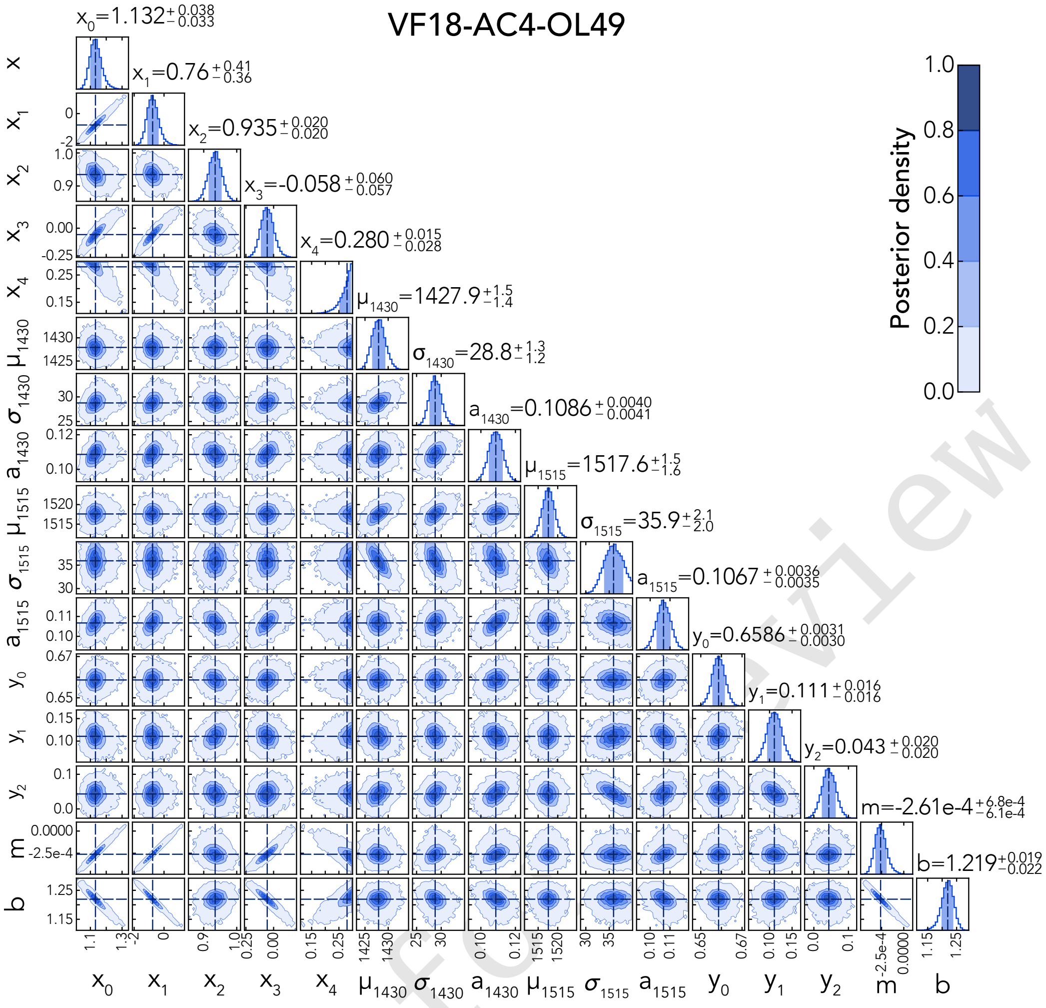

Figure 8: Posterior probability density distribution for the 16 coefficients or parameters of Equation 10 for olivine-hosted melt inclusion VF18-AC4-OL49, fit with PyIRoGlass over 10^6 samples. See Table 2 for additional information about the coefficients and parameters. x_n best-fit coefficients generating the baseline scale the $\overline{\text{Baseline}}$ and $\text{Baseline}_{\text{PC1-4}}$ vectors. y_n best-fit coefficients for fitting the $H_2O_{m,1635}$ peak scale the $\overline{H_2O_{m,1635}}$ and $H_2O_{m,1635_{\text{PC1-2}}}$ vectors. Parameters for fitting the CO_3^{2-} doublet include the subscripted parameters σ, a, and μ; parameters for fitting the linear shift include m and b. Several parameters covary, demonstrating the importance of assessing underlying covariance structures to properly account for uncertainty within this ensemble solution.

sion CN92C-OL2 ($H_2O_{m,1635}$~2.60 wt.%)—highlight the variability observed in the $H_2O_{m,5200}$ peak. Concentrations from the $H_2O_{m,1635}$ peak are tightly constrained, while concentrations from the $H_2O_{m,5200}$ peak vary significantly. Variation within the $H_2O_{m,5200}$ peak concentrations approach 1.00 wt% for D1010 and span over 2.00 wt.% for CN92C-OL2. Some of the variability is captured within the uncertainty of the peak fits, but the reproducibility of $H_2O_{m,1635}$ concentrations allows for greater confidence to be placed in the peak fits. The variability in the data collected from the near-infrared region can be attributed to the small amplitude of the peaks. The stability of the mid-infrared $H_2O_{m,1635}$ peak in the same spectrum is a more significant peak, with respect to the baseline.

Unsaturated glass analyses further allow for analysis of the quality of near-infrared peaks. Reconstructing H2Ot from the combination of either H2Om and the OH^-4500 concentrations allows for a comparison with concentrations determined from the H2Ot, 3550 peak. This comparison reveals that using the $H2O_{m,1635}$ peak results in higher concordance correlation coefficients (CCC), a measure of the agreement between two variables [Lin 1989]. Lower root-mean-square errors (unit-dependent), lower relative root-mean-square errors (unitless), and higher coefficients of determination are also observed (Figure 10C, Figure 10D). The concordance correlation coefficient serves as a more comprehensive measure by capturing both the correlation and agreement between the reconstructed concentrations and the reference. While the coefficient of determination provides information on the proportion of variance in the data explained by the prediction model and the root-mean-square error provides insight into the precision of

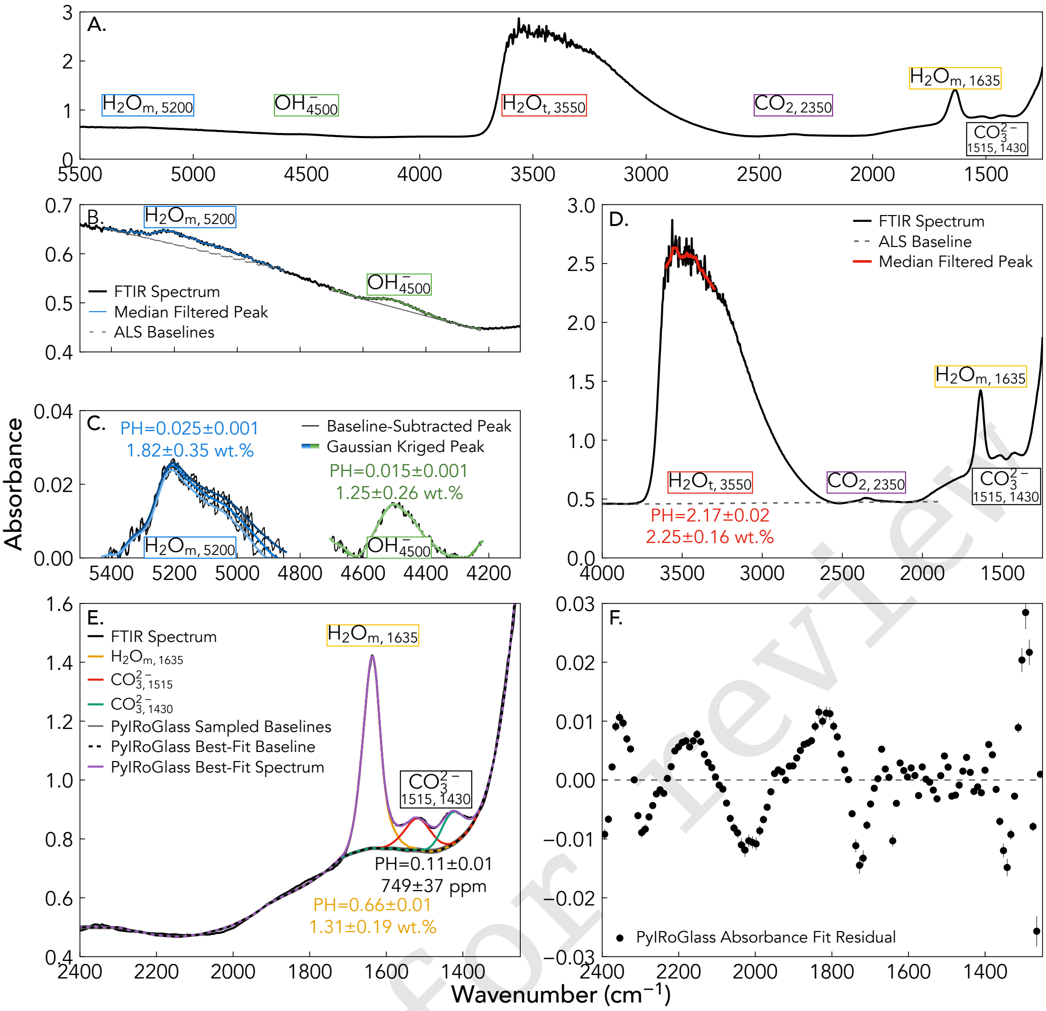

Figure 9: PyIRoGlass baseline and peak fits for the transmission FTIR spectrum of olivine-hosted melt inclusion VF18-AC4-OL49. OL49 has a thickness of 91±3 μm. Uncertainties in peak heights are small within the ensemble solution of PyIRoGlass's fitting framework, and most uncertainties in volatile concentrations are introduced by uncertainties in molar absorptivity and thickness. A. Transmission FTIR spectrum through the near-IR and mid-IR region. OL49's ragged $H_2O_{t,3550}$ peak indicates saturation, prompting the determination of H_2O_t from $H_2O_{m,1635}$ + OH^-_{4500} (see Section 3.4). B. $H_2O_{m,5200}$ and OH^-_{4500} baselines in the near-IR region. Three ALS-derived baselines are generated by sampling slightly different regions around each peak, to assess uncertainty in peak location. C. $H_2O_{m,5200}$ and OH^-_{4500} baseline-subtracted peaks. Mean peak heights with uncertainties are determined from the three baseline-subtracted peaks. D. Saturated $H_2O_{t,3550}$ peak. Three ALS-derived baselines are generated by sampling slightly different regions around each peak, although saturation introduces non-linearity into the Beer-Lambert Law. E. Best-fit baselines and peaks for the $H_2O_{m,1635}$ peak and CO_3^{2-} doublet, with baseline fits over 10^6 samples (grey). $H_2O_{m,1635}$ is lower in concentration than $H_2O_{m,5200}$. H_2O_t equals 2.55±0.16 wt.%, combining $H_2O_{m,1635}$ + OH^-_{4500}. F. Absorbance residual in the best-fit PyIRoGlass spectrum and the FTIR spectrum. Residuals lie between ±0.01 in the wavenumber region beneath the $H_2O_{m,1635}$ peak and CO_3^{2-} doublet.

predictions, neither gives a complete picture of how well predictions agree with actual values. The concordance correlation coefficient integrates both these aspects, ensuring that not only are our predictions closely related to actual values (high correlation) but also that they closely match the actual values (high agreement). Hence, in assessing the accuracy of reconstruction, a higher concordance correlation coefficient serves as a more robust indicator of efficacy. Reconstructing OH^- from the subtraction of either H_2O_m peak from the $H_2O_{t,3550}$ peak and comparing those concentrations against the OH^-_{4500} peak similarly shows that the $H_2O_{m,1635}$ peak yields higher concordance correlation coefficients, lower root-mean-square errors and relative root-mean-square errors, and higher coefficients of determination (Figure 10E, Figure 10F). We recommend use of the $H_2O_{m,1635}$ peak over the $H_2O_{m,5200}$ peak when calculating H_2O_t for saturated samples, due to the better accuracy and precision of the $H_2O_{m,1635}$ peak across sessions.

3.5 Synthetic and Natural Glasses: A Validation Dataset

Two questions remain regarding the performance of PyIRoGlass, as we validate the MCMC technique with Bayesian inference. First, are we reproducing the 'true' devolatilized

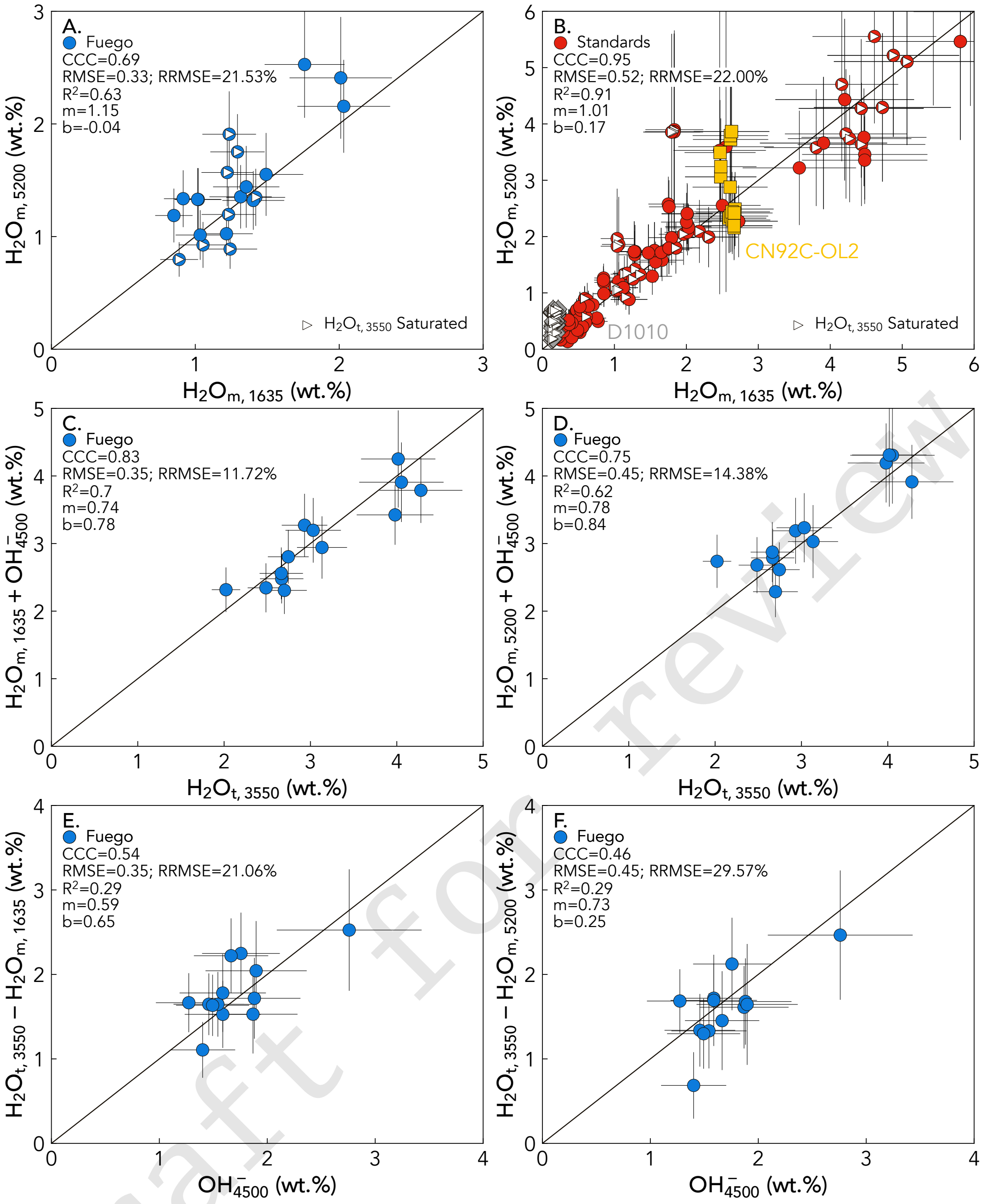

Figure 10: Comparison of the $H_2O_{m,1635}$ and $H_2O_{m,5200}$ peaks. $H_2O_{t,3550}$-saturated glasses are marked with a white triangle. A. $H_2O_{m,1635}$ and $H_2O_{m,5200}$ concentrations in Volcán de Fuego melt inclusions. Most melt inclusion analyses have higher concentrations of $H_2O_{m,5200}$ than $H_2O_{m,1635}$. B. $H_2O_{m,1635}$ and $H_2O_{m,5200}$ concentrations in the internal check standards given in Section 3.2. Most analyses have higher concentrations of $H_2O_{m,5200}$ than $H_2O_{m,1635}$. Significant variability is observed for replicate analyses of internal standards D1010 (grey diamonds) and CN92C-OL2 (yellow squares), forming expansive vertical bands. Note that sample D1010 is saturated in $H_2O_{t,3550}$ despite its low $H_2O_{m,1635}$, due to its thickness of 231 µm and concentration of 0.93±0.10 wt.% H_2O_t. C. H_2O_t from $H_2O_{m,1635}$ + OH^-_{4500}. D. H_2O_t from $H_2O_{m,5200}$ + OH^-_{4500}. E. OH^-_{4500} from $H_2O_{t,3550}$ - $H_2O_{m,1635}$. F. OH^-_{4500} from $H_2O_{t,3550}$ - $H_2O_{m,5200}$.

baseline? We answer this question by comparing PyIRoGlass baselines to a set of experimentally devolatilized ('true') baselines (Table 3, Section *3.5.1*). Second, are we reproducing absolute concentrations? We answer this question by comparing PyIRoGlass results with published values for an array of interlaboratory standards (Table 4, Section *3.5.2*).

3.5.1 *PyIRoGlass Performance on Synthetic Glasses with Devolatilized Baselines*

We assess the performance of PyIRoGlass baselines against the 'true' devolatilized baseline by turning to a validation dataset consisting of 30 synthetic glasses of basaltic, andesitic and basanitic compositions with high H_2O (0.2 to 7.55 wt.%) and CO_2 (0.09 to 1.88 wt.%), each with a corresponding chemistry-and matrix-matched devolatilized glass (Table 3). Experiments were carried out in a piston cylinder apparatus at the Lamont-Doherty Earth Observatory. Run conditions (P-T) varied with each experiment, each lasting 2 hours. For each of the 30 volatilized glasses, we apply PyIRoGlass to the transmission FTIR spectrum to determine the best-fit baseline and peak heights. We then compare these PyIRoGlass peak heights with those determined by using the spectrum of the devolatilized glass with the same chemical composition as the volatilized glass, and a simple subtraction of the devolatilized baseline from the peak absorbances. Replicate analyses of different synthetic glass wafers of variable thickness are included and produce a dataset of 136 spectra, all of which are provided on GitHub.

$CO_{3,1515}^{2-}$ and $CO_{3,1430}^{2-}$ doublet peak heights derived from PyIRoGlass and devolatilized baselines show strong agreement through absorbances of 2.5, within 10% uncertainty bounds (Figure 11A, Figure 11B). Agreement between the samples is demonstrated by the high concordance correlation coefficient, low root-mean-square errors and relative root-mean-square errors, high coefficients of determination, slopes exceeding 0.9, and intercepts approximating 0. Stronger agreement is found between the $CO_{3,1430}^{2-}$ peak heights. This is further demonstrated by examining the ratio between peak heights determined by PyIRoGlass versus the devolatilized baseline, or P/D (Figure 11C, Figure 11D). Scatter (and potentially noise) within the peak heights is demonstrated at peak height absorbances below 0.50 with peak height ratios ranging between 0.86-1.01. Distinct mean peak height ratios ($\overline{P/D}$) of 0.9347 for the $CO_{3,1515}^{2-}$ peak and of 0.9485 for the $CO_{3,1430}^{2-}$ emerge. The similarity between baseline fits—and consequently peak heights—and strength of statistical reproduction suggest that PyIRoGlass properly derives and constructs baselines to fit basaltic to andesitic glasses. There are also some differences between peak heights from PyIRoGlass and devolatilized baselines, notably a 5.5 - 6.5% offset in the two methods (Figure 11C, Figure 11D). A closer examination of the peaks and baselines for the validation dataset can shed light on the causes of this offset (Figure 12).

Baselines from PyIRoGlass and devolatilized methods can be nearly identical (Figure 12A, Figure 12B), but also reveal some meaningful differences (Figure 12C, Figure 12D). Spectrum CI-Ref-6 and CI-Ref-10 (Figure 12A, Figure 12B) demonstrate the success of PyIRoGlass in reconstructing the devolatilized baseline and in fitting the $H_2O_{m,1635}$ peak and Gaussian CO_3^{2-} doublet. PyIRoGlass considers the convolution of the $CO_{3,1515}^{2-}$ peak with the $H_2O_{m,1635}$ peak, resulting in the plotted Gaussian $CO_{3,1515}^{2-}$ not reaching the top of the spectrum. On the other hand, the absorbances determined by simple subtraction of the devolatilized baselines do not account for peak convolution and the contribution of the $H_2O_{m,1635}$ peak. This effect is apparent in the slightly lower $\overline{P/D}$ for $CO_{3,1515}^{2-}$ versus $CO_{3,1430}^{2-}$ (Figure 11C, Figure 11D). The pervasive offset of ~6% (the uniformly lower $\overline{P/D}$ ratio for both CO_3^{2-} peaks) requires a different explanation that involves a mismatch in the baseline. Spectra CI-Ref-Bas-9 and CI-Ref-27 (Figure 12C, Figure 12D) both show greater scooping in the devolatilized baselines than predicted by PyIRoGlass. Such scooping would lead to greater CO_3^{2-} absorbances for both peaks in the devolatilized baseline approach. While this could be a shortcoming of the baseline database input into PyIRoGlass, it could also be an artifact of the experimental procedure, whereby experimental conditions may have altered the chemistry of the devolatilized glass and therefore the baseline. Evidence for this lies in the mismatch between the measured Spectrum CI-Ref-27, and the experimentally devolatilized baseline (Figure 12D), showing a lack of overlap in the region between 1800 and 2300 cm^{-1}. This suggests alterations during the experimental heating that affected the shape of the baseline. The PyIRoGlass ensemble solution, which accounts for a multiplicity of baseline shapes, better matches the measured spectrum for CI-Ref-27. It is possible that experimental devolatilization at a different fO_2 than sample volatilization created a more scooped baseline beneath the CO_3^{2-} doublet. Nonetheless, agreement between baselines from PyIRoGlass and experimental devolatilization within 6% is still highly satisfactory. And PyIRoGlass can continue to be improved by incorporating baselines from a wider array of compositions.

3.5.2 *PyIRoGlass Performance on Published Validation Dataset*

Next, we compare PyIRoGlass concentrations to a validation dataset of interlaboratory glasses with published H_2O and CO_2 concentrations. These include previous studies of volatiles in natural back-arc basin glasses measured by FTIR and SIMS [Pearce et al. 1994; Newman et al. 2000; Rasmussen 2019; Barth 2021; Lytle et al. 2023] or synthetic glasses by FTIR, SIMS, or KFT [Shishkina et al. 2010; Helo et al. 2011; Fiege et al. 2015; Brounce et al. 2021]. Natural glasses include back-arc basin basalts D1010, ALV1833-11, WOK5-4, and ALV1846-9 analyzed with FTIR by Newman et al. [2000]; CD33-12-2-2 and CD33-22-1-1 analyzed with SIMS by Lytle et al. [2023]; ETFSR-OL8 analyzed with SIMS by Barth [2021]. Back-arc basin glasses analyzed with FTIR utilize baselines from a least squares fitting technique, using a single reference baseline and peak components, described by Newman et al. [2000]. Synthetic glasses include the high-Mg basaltic glasses ABWCl-F0x and ABWB-0x analyzed with KFT for H_2O by Fiege et al. [2015]; boninites BF73, BF76, and BF77 analyzed with KFT for H_2O and elemental analyzer (EA) for CO_2 by Brounce et al. [2021]; basalts M35 and M43 analyzed with KFT for H_2O and FTIR for CO_2 by Shishkina et al. [2010]; basalt NS-1 analyzed with FTIR for H_2O and CO_2 by Helo et al. [2011]. Utilizing PyIRoGlass to process the transmission spectra of previously published samples allow for the validation of concentration measurements. Glasses analyzed with SIMS, KFT, and EA allow for comparison against more independent analytical techniques, although many calibrations rely on standards analyzed by FTIR.

Application of PyIRoGlass to the validation dataset shows that H_2O_t determined by FTIR primarily agree with published values up to concentrations of approximately 4.5 wt.%, even when the $H_2O_{t,3550}$ peak is saturated and we calculate H_2O_t from the $H_2O_{m,1635}$ and OH_{4500}^- peaks (Fig-

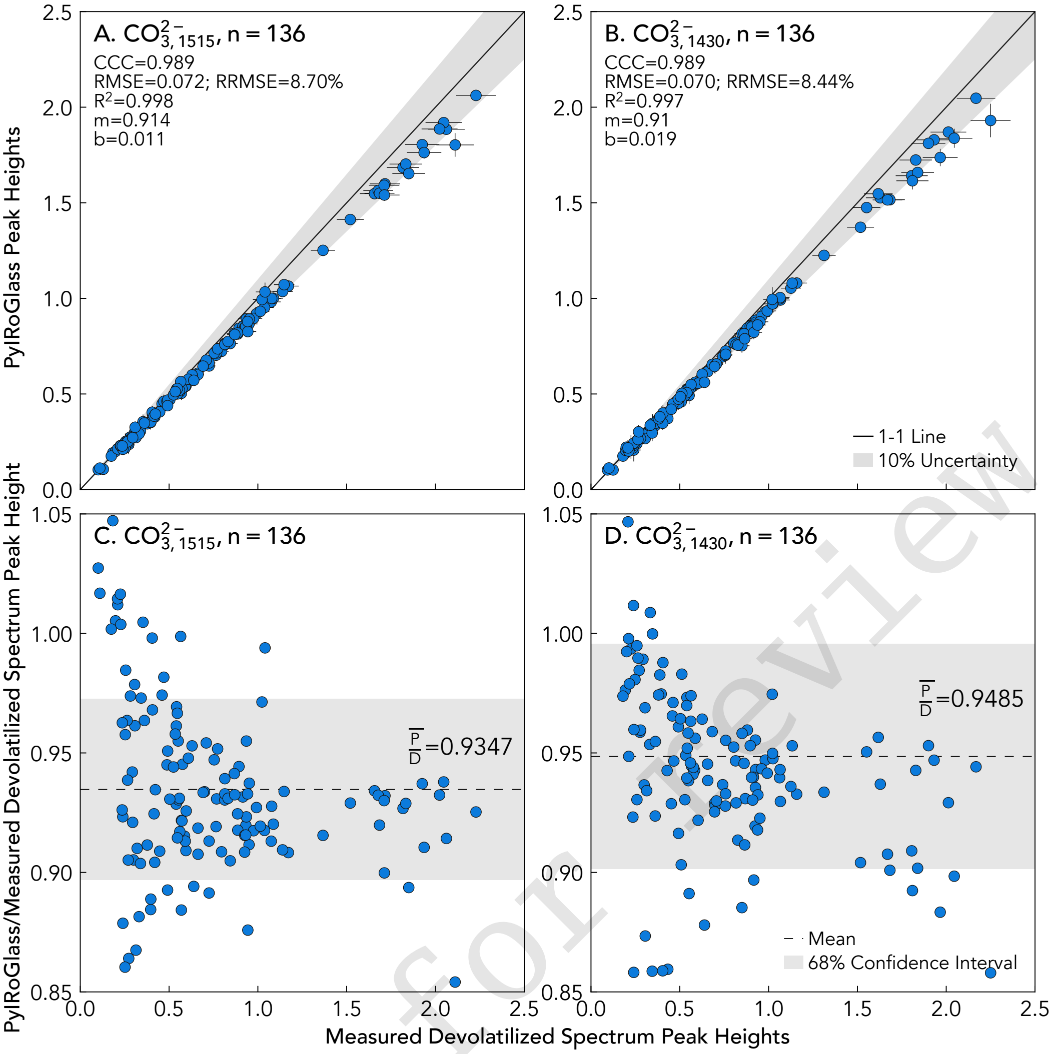

Figure 11: Peak heights between PyIRoGlass and devolatilized baselines for synthesized basalt, andesite, and basanite glasses (Table 3). Peak heights are all normalized to a thickness of 50 µm to demonstrate the significant range of concentrations. 1 sigma peak height uncertainties from PyIRoGlass are plotted, along with 5% uncertainty imposed on peak heights from the devolatilized method. A. Peak heights for $CO_{3,1515}^{2-}$. B. Peak heights for $CO_{3,1430}^{2-}$. All PyIRoGlass peak heights fall within 10% uncertainty of the devolatilized peak heights, with the $CO_{3,1430}^{2-}$ showing stronger agreement. C. Ratio of peak heights generated by the two methods for $CO_{3,1515}^{2-}$, with a mean ratio of 0.9347. D. Peak height ratios for $CO_{3,1430}^{2-}$, with a mean ratio of 0.9485. Peak height ratios at lower absorbances incorporate more significant noise.

ure 13A). Agreement between concentrations is demonstrated by the high concordance correlation coefficient, low root-mean-square error and relative root-mean-square error of ~13%, high coefficient of determination, slope nearing 1, and intercept nearing 0. The calculated H_2O_t from glasses synthesized by Fiege et al. [2015] are well represented by the combined $H_2O_{m,1635}$ and OH^-_{4500} concentrations despite saturation, discussed in Section 3.4. Offsets observed in back-arc basin glasses D1010, ALV1833-11, WOK5-4, and ALV1846-9 can likely be attributed to differences in fitting methodologies, fitting regions, and potential heterogeneity in analyzed glass wafers. Molar absorptivities from our inversion agree within 1 $L \cdot mol^{-1} \cdot m$ with published and utilized molar absorptivities of 63 $L \cdot mol^{-1} \cdot m$. The remaining samples within the validation dataset agree within the uncertainties of analysis at concentrations below 4.5 wt.% H_2O_t, across two distinct analytical techniques (KFT and SIMS). Hauri et al. [2002] demonstrate a linear H_2O calibration across basalt, andesites, and rhyolites below 1.5 wt.% H_2O. Non-linearities and curved calibrations emerge as H_2O surpasses 1.5 wt.%, with the additional introduction of compositional dependencies. For this reason, further analyses of standards with higher H_2O concentrations would be welcomed.

PyIRoGlass demonstrates strong agreement in CO_2 determined by FTIR, SIMS, and EA through concentrations of 4000 ppm for back-arc basin and synthetic glasses (Figure 13B). We focus here on low-H_2O glasses, as we verified the suppression effect of H_2O on CO_2 reported by Hervig et al. [2009] for SIMS measurements made by the Cs^+ beam. This effect is minimal for samples with less than 3 wt.% H_2O, so we con-

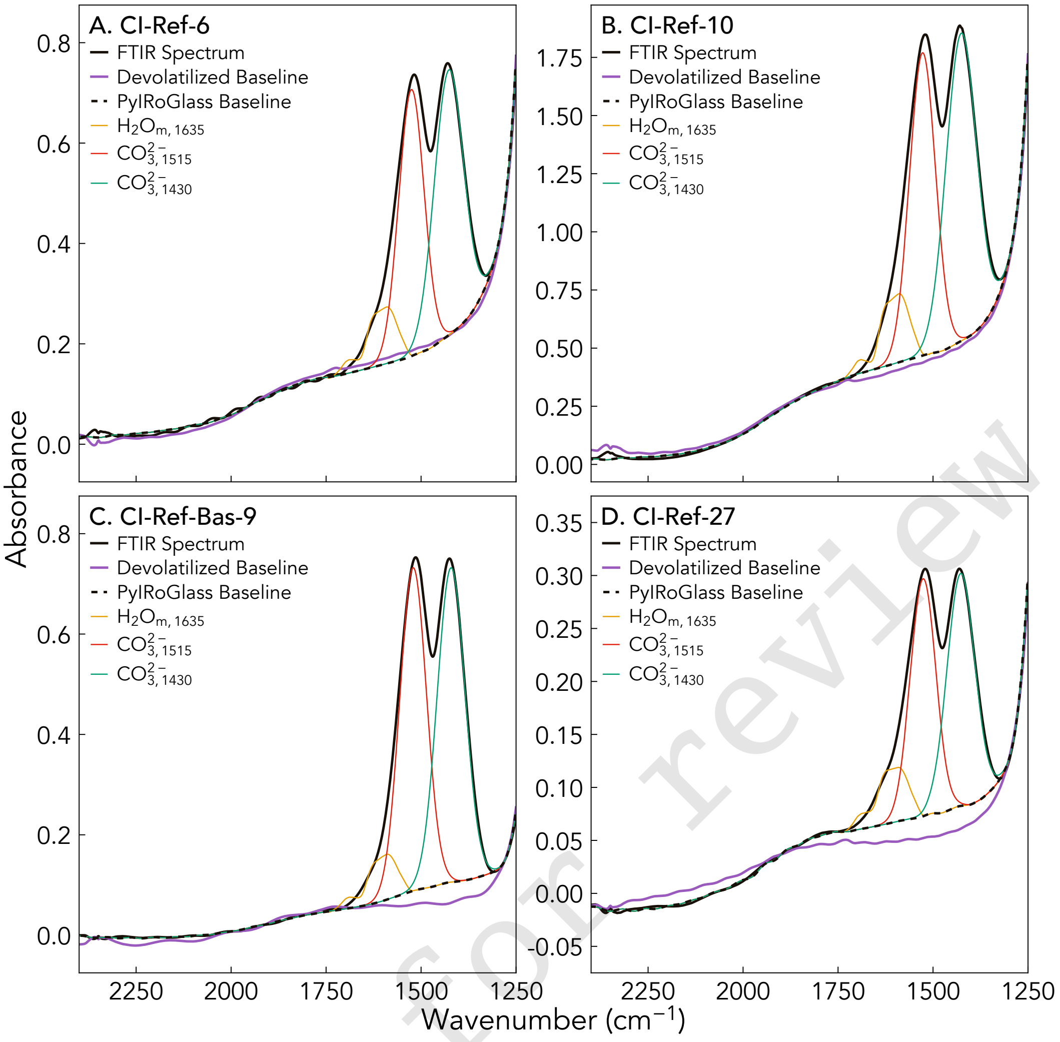

Figure 12: Comparison of PyIRoGlass and devolatilized baselines for four exemplar spectra. Spectra are presented as analyzed, without thickness normalization. A. CI-Ref-6 with strong baseline agreement, B. CI-Ref-10 with strong baseline agreement. C. CI-Ref-Bas-9 with the devolatilized baseline accommodating greater scooping beneath CO_3^{2-} peaks. D. CI-Ref-27 with the devolatilized baseline accommodating greater scooping beneath CO_3^{2-} peaks, but divergence of baselines past 1800 cm^{-1}.

sidered this cut-off in our comparison with published SIMS data (Figure 13B). Thus, our results are restricted to synthetic boninites BF73, BF76, BF77 and synthetic basalt NS-1, along with a suite of natural, low H_2O and low CO_2 back-arc basin basalts. For glasses with published concentrations using FTIR, we use the molar absorptivities provided in each respective study to calculate concentrations. This is for the sake of consistency, to highlight the baseline fitting in PyIRoGlass, our primary objective. If we used the compositionally-dependent molar absorptivities in Figure 5, results would be ~30% lower for the Brounce et al. [2021] BF glasses and ~12% higher for the Helo et al. [2011] NS-1 glass. Clearly, more work resolving the compositional effects on the molar absorptivity of the CO_2 peaks is welcome. Overall, strong agreement in CO_2 concentrations between PyIRoGlass and the other published results (Figure 13B) is demonstrated by the high concordance correlation coefficient, low root-mean-square error and relative root-mean-square error of ~9%, high coefficient of determination, slope nearing 1, and intercept nearing 0.

3.6 Chemistry Modulating the Baseline

Here, we explore the relationships between glass chemistry and the baseline in our test and validation datasets. Correlation coefficients between chemical components and the best-fit baseline-generating coefficients from PyIRoGlass are low, but these weak correlations may still provide some information. The parameters impacting the baseline most significantly similarly modify melt polymerization and structure—including the network-forming tetrahedrally coordinated cations in SiO_2, Al_2O_3, and minor components Fe_2O_3 and TiO_2; the network-modifying alkali earth cations in CaO and MgO; silicate network-depolymerizing H_2O (Figure 14). Notably, the commonly used parameter of non-bridging oxygens to tetrahedral cations (NBO/T) does not strongly correlate with any baseline-generating coefficient, while the individual network-forming, network-modifying, and network-depolymerizing components do [Mysen and Richet 2018; Mysen 2022].

Table 3: Glass standards with devolatilized baselines in the validation dataset. Experiments performed by piston cylinder and analyses performed with the Thermo Scientific Nicolet iN10 MX Fourier Transform Infrared Spectrometer, both at the Lamont-Doherty Earth Observatory. Provided uncertainties propagate analytical, fitting, and replicate uncertainties. Peak heights are normalized to 50 μm.

Sample	Composition	n	$CO_{2,1515}$ Devolatilized Peak Height	PyIRoGlass $CO_{2,1515}$ Peak Height	$\sigma CO_{2,1515}$ Peak Height	$CO_{2,1430}$ Devolatilized Peak Height	PyIRoGlass $CO_{2,1430}$ Peak Height	$\sigma CO_{2,1515}$ Peak Height	PyIRoGlass H_2O (wt.%)	σPyIRoGlass H_2O (wt.%)	PyIRoGlass CO_2 (ppm)	σPyIRoGlass CO_2 (ppm)
CI-LMT-BA3	Synthetic Basaltic Andesite	1	1.040	1.034	0.012	1.021	0.995	0.016	0.435	0.107	10133	1691
CI-LMT-BA4	Synthetic Basaltic Andesite	1	1.367	1.251	0.006	1.312	1.225	0.007	0.325	0.037	12376	836
CI-LMT-BA17	Synthetic Basaltic Andesite	2	2.145	1.973	0.125	2.090	1.958	0.125	0.228	0.050	18759	1757
CI-Ref-4	Synthetic MORB	2	1.007	0.924	0.040	0.992	0.938	0.046	1.112	0.107	8749	536
CI-Ref-6	Synthetic MORB	7	0.561	0.520	0.013	0.549	0.521	0.017	1.026	0.095	4865	250
CI-Ref-8	Synthetic MORB	5	0.930	0.858	0.044	0.913	0.862	0.044	0.882	0.097	8836	637
CI-Ref-9	Synthetic MORB	2	0.909	0.836	0.024	0.883	0.832	0.025	1.608	0.134	8778	422
CI-Ref-10	Synthetic MORB	8	0.626	0.574	0.070	0.635	0.597	0.109	0.802	0.073	5356	853
CI-Ref-11	Synthetic MORB	3	0.768	0.705	0.059	0.751	0.704	0.063	1.051	0.181	6526	830
CI-Ref-14	Synthetic MORB	2	0.349	0.318	0.038	0.330	0.307	0.039	1.070	0.150	2900	462
CI-Ref-15	Synthetic MORB	3	0.275	0.250	0.023	0.247	0.232	0.034	1.005	0.306	2282	565
CI-Ref-18	Synthetic MORB	5	0.303	0.286	0.038	0.293	0.280	0.031	1.007	0.137	2648	373
CI-Ref-20	Synthetic MORB	5	0.310	0.296	0.035	0.299	0.287	0.035	0.777	0.103	2714	375
CI-Ref-23	Synthetic MORB	3	0.252	0.231	0.021	0.242	0.231	0.013	1.001	0.093	2178	191
CI-Ref-24	Synthetic MORB	3	0.114	0.108	0.007	0.106	0.106	0.009	0.975	0.116	994	89
CI-Ref-25	Synthetic MORB	10	0.993	0.916	0.124	0.982	0.925	0.126	0.863	0.187	7848	1918
CI-Ref-27	Synthetic MORB	6	0.581	0.546	0.072	0.570	0.543	0.077	1.142	0.190	5088	806
CI-Ref-28	Synthetic MORB	5	0.976	0.904	0.089	0.961	0.906	0.090	1.350	0.155	8514	1022
CI-Ref-Bas-3	Synthetic Basanite (El Hierro)	7	0.682	0.643	0.072	0.675	0.626	0.070	1.510	0.251	6723	945
CI-Ref-Bas-4	Synthetic Basanite (El Hierro)	1	0.183	0.192	0.005	0.193	0.189	0.006	1.425	0.154	2011	135
CI-Ref-Bas-5	Synthetic Basanite (El Hierro)	3	0.195	0.196	0.020	0.199	0.195	0.020	1.645	0.185	2078	247
CI-Ref-Bas-6	Synthetic Basanite (El Hierro)	3	0.937	0.861	0.119	0.930	0.848	0.112	1.688	0.227	9290	1486
CI-Ref-Bas-7	Synthetic Basanite (El Hierro)	5	0.410	0.381	0.064	0.400	0.375	0.057	1.399	0.241	4067	768
CI-Ref-Bas-8	Synthetic Basanite (El Hierro)	6	0.459	0.431	0.063	0.464	0.423	0.061	1.329	0.212	4403	746
CI-Ref-Bas-9	Synthetic Basanite (El Hierro)	6	0.850	0.794	0.090	0.849	0.781	0.085	1.480	0.773	10650	2912
ND70-2	Synthetic MORB	2	0.218	0.221	0.014	0.199	0.213	0.015	3.799	0.630	1998	237
ND70-3	Synthetic MORB	7	0.259	0.248	0.040	0.229	0.237	0.036	3.433	0.967	2226	403
ND70-4	Synthetic MORB	8	0.474	0.446	0.066	0.440	0.427	0.060	3.861	0.886	4095	621
ND70-5	Synthetic MORB	6	1.846	1.725	0.164	1.743	1.652	0.155	7.550	0.900	16250	1967
ND70-6	Synthetic MORB	9	1.793	1.630	0.124	1.843	1.647	0.172	6.055	1.012	15370	1969

Table 4: Back-arc basin glasses (BAB), melt inclusions (MI), and synthetic basaltic glasses, within the validation dataset with stated sources — both in terms of publication and locality. Published analytical technique and locations — FTIR at California Institute of Technology (Caltech) fits baselines with the Newman et al. [2000] least squares fitting technique with a single baseline and $H_2O_{m,1635}$ peak component; FTIR at Institut für Mineralogie, Leibniz Universität Hannover (Hannover) fits tangential baselines; FTIR at American Museum of Natural History (AMNH) fits a devolatilized baseline; SIMS analyses performed at Carnegie Institution for Science (CIS) and Centre de Recherches Pétrographiques et Géochimiques, Université de Lorraine (Nancy). Volatile concentrations and uncertainties are presented as provided within the reference within the published concentration column. 10% uncertainty is imposed when uncertainties are not reported, or where published uncertainties are unrealistic given inherent uncertainties (thickness and molar absorptivity in FTIR). - indicates that there is no published measurement or uncertainty, and bdl indicates that concentrations were below detection limits.

Sample	Reference	Composition	Published Analytical Technique	Published H_2O (wt.%)	Published σH_2O (wt.%)	PyIRoGlass H_2O (wt.%)	PyIRoGlass σH_2O (wt.%)	Published CO_2 (ppm)	Published σCO_2 (ppm)	PyIRoGlass CO_2 (ppm)	PyIRoGlass σCO_2 (ppm)	PyIRoGlass CO_2 (ppm) with published ε	PyIRoGlass σCO_2 (ppm) with published ε
ABWCl-F0x	Fiege et al. [2015]	Synthetic High-Mg Basalt	FTIR-Hannover	2.97	0.29	3.19	0.48	-	-	429	16	-	-
ABWB-0x	Fiege et al. [2015]	Synthetic High-Mg Basalt	KFT-Hannover	4.40	0.40	3.88	0.49	-	-	1384	44	-	-
ALV1833-11	Newman et al. [2000]	BAB-Mariana Trough	FTIR-Caltech	1.20	0.01	1.02	0.08	102	12	34	9	33	9
21ALV1846-9	Newman et al. [2000]	BAB-Mariana Trough	FTIR-Caltech	1.89	0.05	1.45	0.11	bdl	bdl	bdl	bdl	bdl	bdl
BF73	Brounce et al. [2021]	Synthetic Boninite	KFT/EA/FTIR-Hannover	0.715	0.07	0.82	0.06	2995	190	2380	65	3042	84
BF76	Brounce et al. [2021]	Synthetic Boninite	KFT/EA/FTIR-Hannover	0.669	0.07	0.75	0.06	2336	127	1814	54	2319	68
BF77	Brounce et al. [2021]	Synthetic Boninite	KFT/EA/FTIR-Hannover	0.696	0.07	0.86	0.08	1030	27	697	37	891	47
CD33-12-2-2	Pearce et al. [1994];Lytle et al. [2023]	BAB-Lau Basin	SIMS-CIS	0.27	0.03	0.27	0.02	170	-	129	14	-	-
CD33-22-1-1	Pearce et al. [1994];Lytle et al. [2023]	BAB-Lau Basin	SIMS-CIS	0.49	0.05	0.53	0.04	109	-	66	16	-	-
D1010	Newman et al. [2000]	BAB-Mariana Trough	FTIR-Caltech	1.13	0.07	0.93	0.10	139	1	177	7	149	6
ETFSR-OL8	Barth [2021]	MI-Etna	SIMS-Nancy	4.47	0.45	3.85	0.43	-	-	5218	324	-	-
M35	Shishkina et al. [2010]	Synthetic Basalt	KFT/FTIR-Hannover	4.20	0.12	4.10	0.45	1019	81	961	72	1000	75
M43	Shishkina et al. [2010]	Synthetic Basalt	KFT/FTIR-Hannover	2.62	0.11	2.52	0.25	3172	265	2694	145	2857	154
NS-1	Helo et al. [2011]	Synthetic Basalt	FTIR-AMNH	0.37	0.04	0.35	0.03	3154	-	4218	154	3546	129
23WOK5-4	Newman et al. [2000]	BAB-Mariana Trough	FTIR-Caltech	1.60	0.05	1.01	0.08	64	6	21	6	18	5

Increasing the proportion of network-forming cations in SiO_2 and Al_2O_3, sitting near the center of oxygen tetrahedra, appears to increase x_0 or the best-fit coefficient altering the amplitude of the $\overline{\text{Baseline}}$. The curvature of the baseline captured by x_1, which scales $\overline{\text{Baseline}}_{\text{PC1}}$, can be described by the depolymerization of the melt and the decrease of NBO/T due to the increase of minor network-forming cations Fe_2O_3 and TiO_2 and depolymerizer H_2O. Variations in oxidation state alter the extent of polymerization, with the oxidation of Fe^{2+} to Fe^{3+} increasing the NBO/T of the melt [Dingwell and Virgo 1987; Mysen 2022]. This relationship between oxidation state, extent of polymerization, and the baseline potentially

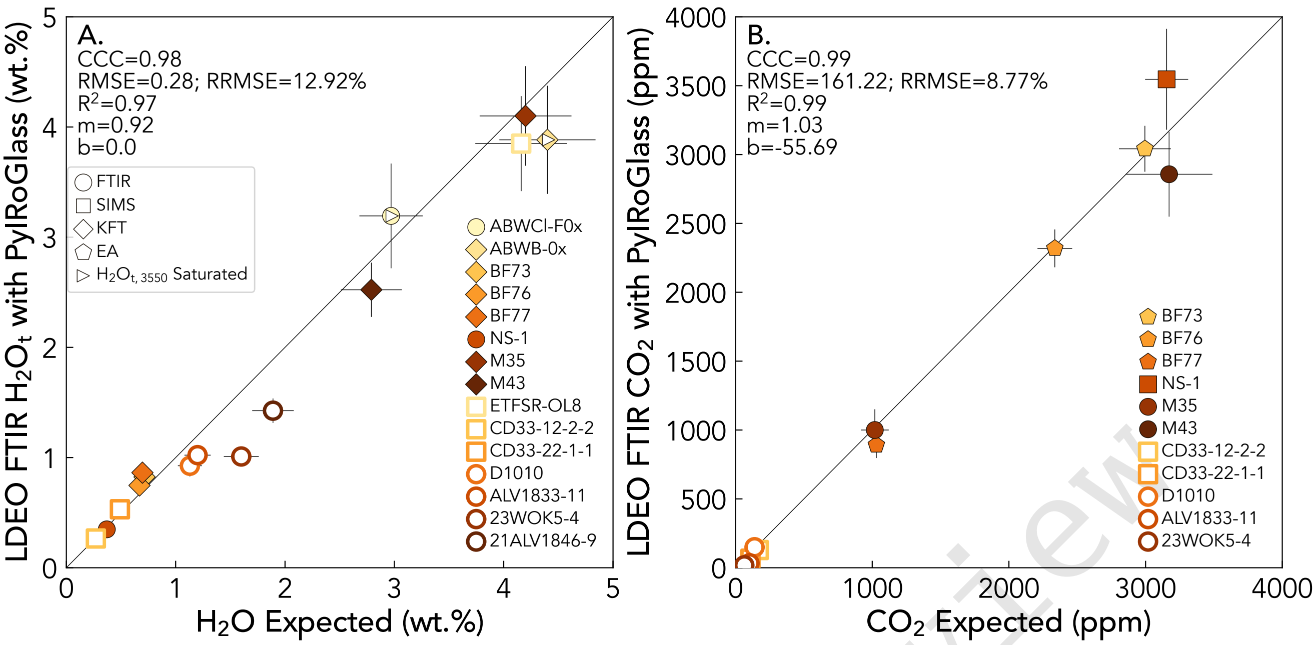

Figure 13: Comparison of volatile concentrations from PyIRoGlass and concentrations from published analyses by FTIR, SIMS, KFT, or EA. A. H_2O concentrations from FTIR vs. concentrations from FTIR or SIMS. Saturated samples H_2O concentrations are represented by combining $H_2O_{m,1635}$ and OH^-_{4500}. Agreement within H_2O concentrations is demonstrated by the high CCC, low RMSE (wt.% unit), low RRMSE (unitless), high R^2, m nearing 1, and b nearing 0. 1 sigma uncertainties are reported from PyIRoGlass. B. CO_2 concentrations by FTIR vs. concentrations from FTIR or SIMS. We use the molar absorptivities provided in each respective study to calculate CO_2 concentrations, for samples with published concentrations from FTIR, presented in Table 4. 2 sigma uncertainties from PyIRoGlass are reported.

demonstrates some unintentional consequences for utilizing devolatilized baselines for fitting natural samples, since the experimental process of devolatilizing glasses can alter their oxidation state. x_2 does not offer clear insights into the characteristics of the melt. x_3, scaling $\overline{\text{Baseline}}_{\text{PC3}}$, demonstrates the same trends as x_1, but with stronger correlation coefficients for H_2O and density. x_4, scaling $\overline{\text{Baseline}}_{\text{PC4}}$, demonstrates the same trends as x_1 and x_3, but with the additional impact of network-modifying cations. Decreasing the proportion of network-modifying cations MgO and CaO, which charge balance tetrahedrally coordinated Al^{3+}, increases the amplitude of x_4 [Mysen and Virgo 1986; Mysen 2022].

While the chemical variability of the glasses in the test and validation dataset provide some insight into the nature of the baseline, the baseline cannot be explicitly generated or empirically fit from solely glass chemistry. The necessity of ensemble solutions such as PyIRoGlass is underscored by the lack of a straightforward correlation between the baseline with chemistry within this test and validation dataset. A full understanding of these relationships remains elusive and is beyond the scope of this paper. The publication and availability of more FTIR spectra for glasses with a wide range of chemical compositions will allow for further exploration.

4 CONCLUSIONS

PyIRoGlass is a novel Bayesian method with MCMC sampling developed and validated for the purpose of reproducibly processing the transmission FTIR spectra of basaltic to andesitic glasses, where carbon is primarily dissolved as CO_3^{2-}, in the open-source Python language. The utility of PyIRoGlass emerges when devolatilized baselines are not readily available, which is particularly true of melt inclusion studies. All parameters within the Beer-Lambert Law—including the baseline, molar absorptivity, thickness, and density—are closely examined to quantify their associated uncertainties. Inverting for molar absorptivity as a function of compositional parameter properly quantifies both the uncertainty of the inversion and of the composition. PyIRoGlass allows for the sampling of all likely baselines and peaks to iteratively solve for the best-fit parameters, in order to determine volatile concentrations with robust estimates of uncertainties.

PyIRoGlass is currently tuned to arc basalts and andesites; future work could identify the shapes and variability in the baselines for other compositions such as alkali basalts and rhyolites. The performance of PyIRoGlass is dependent on the model and calibration inputs, with the input degassed transmission FTIR spectra fundamentally determining the shape and variability of the baseline. As the dataset of degassed spectra expands, our understanding of the shape and variability of the baseline might shift to fit a wider array of compositions. Composition-dependent calibrations of molar absorptivity might similarly change as datasets evolve. Open-sourcing this Python code encourages iterative development and enhancement. Future validation may target the synthesis and analysis of high volatile glasses, to resolve the disagreements between volatile analyses by FTIR and SIMS. Further

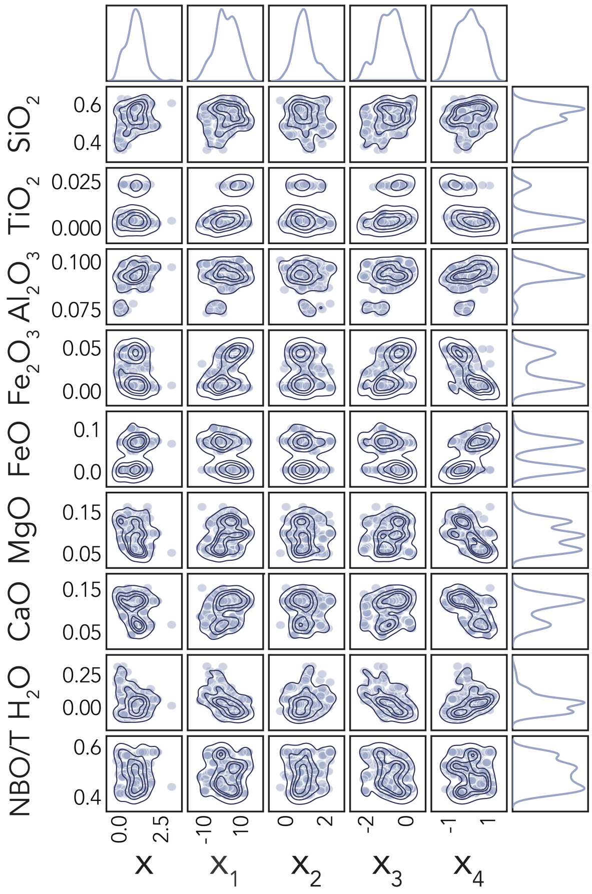

Figure 14: Best-fit distributions of the baseline-generating coefficients, including x_0 scaling $\overline{\text{Baseline}}$ and x_{1-4} scaling $\overline{\text{Baseline}}_{\text{PC1-4}}$, and chemical composition of the melt in the test and validation datasets. x_0 is weakly correlated with SiO_2 and Al_2O_3. x_1 is correlated with Fe_2O_3, FeO, TiO_2, and H_2O. x_2 is uncorrelated. x_3 is correlated with Fe_2O_3, FeO, and H_2O. x_4 is correlated with Fe_2O_3, FeO, MgO, CaO, and H_2O.

development of PyIRoGlass will focus on the expansion of this open-source package for processing rhyolitic glasses, where carbon is primarily dissolved as CO_2.

AUTHOR CONTRIBUTIONS

SS, HT, TP, and AB conceived the project. SS wrote the manuscript, collected the Fuego melt inclusion test dataset and most of the standard validation dataset, developed most of the Python code, documented the code, and interpreted the results. HT performed the principle component analysis for fitting the CO_3^{2-} doublet and $H_2O_{m,1635}$ peak and wrote the initial MCMC parameter fitting code. TP helped scope the devolatilized baseline approach, provided guidance and support, and edited the manuscript. AB helped with data collection and interpretation, and tested the code. DR analyzed and provided the database of devolatilized melt inclusions. YM and HL synthesized, analyzed, and provided high volatile glasses for validation. HL tested the code. WM developed the inversion code with SS for determining absorption coefficients and critically contributed to understandings of robust uncertainty/error analysis. All authors provided feedback on the results and manuscript.

ACKNOWLEDGEMENTS

We extend our gratitude to Renat Almeev, Alexander Lloyd, François Holtz, Katherine Kelley, Sally Newman, and Tatiana Shishkina for providing glasses analyzed by FTIR in the validation dataset. Elizabeth Cottrell generously provided FTIR spectra of the back-arc basin glasses from the Mariana Trough and Lau Basin in the validation dataset. Shuo (Echo) Ding assisted with the FTIR analyses of the BF samples and Céline Martin was instrumental in supporting EPMA analyses of both test and validation datasets. Our appreciation also goes to Penny Wieser for facilitating this package's availability on PyPi and ReadTheDocs and for guidance on unit testing.

DATA AVAILABILITY

All data and code are available on GitHub (github.com/sarahshi/PyIRoGlass), with documentation and examples at Read The Docs (pyiroglass.readthedocs.io). The code can be run through the Google Colab cloud server. The supplement contains information on the inversion technique and analytical methodology.

COPYRIGHT NOTICE

REFERENCES

Acocella, J., M. Tomozawa, and E. Watson (1984). "The nature of dissolved water in sodium silicate glasses and its effect on various properties". *Journal of Non-Crystalline Solids* 65(2-3), pages 355–372. DOI: `10.1016/0022-3093(84)90058-9`.

Allabar, A. and M. Nowak (2020). "(High spatial resolution analysis of H_2O in silicate glass using attenuated total reflection FTIR spectroscopy coupled with a focal plane array detector)". *Chemical Geology* 556, page 119833. DOI: `10.1016/j.chemgeo.2020.119833`.

Allison, C. M., K. Roggensack, and A. B. Clarke (2019). "H_2O–CO_2 solubility in alkali-rich mafic magmas: new experiments at mid-crustal pressures". *Contributions to Mineralogy and Petrology* 174(7), pages 1–24. DOI: `10.1007/s00410-019-1592-4`.

Aubaud, C., H. Bureau, C. Raepsaet, H. Khodja, A. C. Withers, M. M. Hirschmann, and D. R. Bell (2009). "Calibration of the infrared molar absorption coefficients for H in olivine, clinopyroxene and rhyolitic glass by elastic recoil detection analysis". *Chemical Geology* 262(1-2), pages 78–86. DOI: `10.1016/j.chemgeo.2009.01.001`.

Barth, A. (2021). “Ascent rates and volatiles of explosive basaltic volcanism”. PhD thesis. Columbia University in the City of New York. DOI: `10.7916/d8-zkzt-a130`.

Behrens, H. (1995). “Determination of water solubilities in high-viscosity melts: an experimental study on $NaAlSi_3O_8$ and $KAlSi_3O_8$ melts”. *European Journal of Mineralogy*, pages 905–920. DOI: `10.1127/ejm/7/4/0905`.

Behrens, H., V. Misiti, C. Freda, F. Vetere, R. E. Botcharnikov, and P. Scarlato (2009). “Solubility of H_2O and CO_2 in ultrapotassic melts at 1200 and 1250°C and pressure from 50 to 500 MPa”. *American Mineralogist* 94(1), pages 105–120. DOI: `10.2138/am.2009.2796`.

Behrens, H., C. Romano, M. Nowak, F. Holtz, and D. B. Dingwell (1996). “Near-infrared spectroscopic determination of water species in glasses of the system MAlSi3O8 (M= Li, Na, K): an interlaboratory study”. *Chemical Geology* 128(1-4), pages 41–63. DOI: `10.1016/0009-2541(95)00162-X`.

Blundy, J. and K. Cashman (2001). “Ascent-driven crystallisation of dacite magmas at Mount St Helens, 1980–1986”. *Contributions to Mineralogy and Petrology* 140(6), pages 631–650. DOI: `doi.org/10.1007/s004100000219`.

Branch, M. A., T. F. Coleman, and Y. Li (1999). “A Subspace, Interior, and Conjugate Gradient Method for Large-Scale Bound-Constrained Minimization Problems”. *SIAM Journal on Scientific Computing* 21(1), pages 1–23. DOI: `10.1137/S1064827595289108`.

Brooker, R., S. Kohn, J. Holloway, and P. McMillan (2001a). “Structural controls on the solubility of CO_2 in silicate melts: part I: bulk solubility data”. *Chemical Geology* 174(1-3), pages 225–239. DOI: `10.1016/S0009-2541(00)00353-3`.

– (2001b). “Structural controls on the solubility of CO_2 in silicate melts: part II: IR characteristics of carbonate groups in silicate glasses”. *Chemical Geology* 174(1-3), pages 241–254. DOI: `10.1016/S0009-2541(00)00318-1`.

Brounce, M., M. K. Reagan, K. A. Kelley, E. Cottrell, K. Shimizu, and R. Almeev (2021). “Covariation of slab tracers, volatiles, and oxidation during subduction initiation”. *Geochemistry, Geophysics, Geosystems* 22(6), e2021GC009823. DOI: `10.1029/2021GC009823`.

Carroll, M. R. and J. G. Blank (1997). “The solubility of H_2O in phonolitic melts”. *American Mineralogist* 82(5-6), pages 549–556. DOI: `10.2138/am-1997-5-615`.

Carvajal, R. C., L. E. Arias, H. O. Garces, and D. G. Sbarbaro (2016). “Comparative analysis of a principal component analysis-based and an artificial neural network-based method for baseline removal”. *Applied Spectroscopy* 70(4), pages 604–617. DOI: `10.1177/0003702816631293`.

Cressie, N. (1990). “The origins of kriging”. *Mathematical geology* 22, pages 239–252. DOI: `10.1007/BF00889887`.

Cubillos, P., J. Harrington, T. J. Loredo, N. B. Lust, J. Blecic, and M. Stemm (2017). “On Correlated-noise Analyses Applied to Exoplanet Light Curves”. *The Astronomical Journal* 153(1), page 3. DOI: `10.3847/1538-3881/153/1/3`.

Di Matteo, V., M. Carroll, H. Behrens, F. Vetere, and R. Brooker (2004). “Water solubility in trachytic melts”. *Chemical Geology* 213(1-3), pages 187–196. DOI: `10.1016/j.chemgeo.2004.08.042`.

Di Matteo, V., A. Mangiacapra, D. Dingwell, and G. Orsi (2006). “Water solubility and speciation in shoshonitic and latitic melt composition from Campi Flegrei Caldera (Italy)”. *Chemical Geology* 229(1-3), pages 113–124. DOI: `10.1016/j.chemgeo.2006.01.015`.

Dingwell, D. B. and D. Virgo (1987). “The effect of oxidation state on the viscosity of melts in the system Na2O-FeO-Fe2O3-SiO2”. *Geochimica et Cosmochimica Acta* 51(2), pages 195–205. DOI: `10.1016/0016-7037(87)90231-6`.

Dixon, J. E. and D. A. Clague (2001). “Volatiles in basaltic glasses from Loihi Seamount, Hawaii: Evidence for a relatively dry plume component”. *Journal of Petrology* 42(3), pages 627–654. DOI: `10.1093/petrology/42.3.627`.

Dixon, J. E. and V. Pan (1995). “Determination of the molar absorptivity of dissolved carbonate in basanitic glass”. *American Mineralogist* 80(11-12), pages 1339–1342. DOI: `10.2138/am-1995-11-1224`.

Dixon, J. E., E. Stolper, and J. R. Delaney (1988). “Infrared spectroscopic measurements of CO_2 and H_2O in Juan de Fuca Ridge basaltic glasses”. *Earth and Planetary Science Letters* 90(1), pages 87–104. DOI: `10.1016/0012-821X(88)90114-8`.

Dixon, J. E. and E. M. Stolper (1995). “An experimental study of water and carbon dioxide solubilities in mid-ocean ridge basaltic liquids. Part II: applications to degassing”. *Journal of Petrology* 36(6), pages 1633–1646. DOI: `10.1093/oxfordjournals.petrology.a037268`.

Dixon, J. E., E. M. Stolper, and J. R. Holloway (1995). “An experimental study of water and carbon dioxide solubilities in mid-ocean ridge basaltic liquids. Part I: calibration and solubility models”. *Journal of Petrology* 36(6), pages 1607–1631. DOI: `10.1093/oxfordjournals.petrology.a037267`.

Dobson, P. F., S. Epstein, and E. M. Stolper (1989). “Hydrogen isotope fractionation between coexisting vapor and silicate glasses and melts at low pressure”. *Geochimica et Cosmochimica Acta* 53(10), pages 2723–2730. DOI: `10.1016/0016-7037(89)90143-9`.

Duncan, M. S. and R. Dasgupta (2015). “Pressure and temperature dependence of CO_2 solubility in hydrous rhyolitic melt: implications for carbon transfer to mantle source of volcanic arcs via partial melt of subducting crustal lithologies”. *Contributions to Mineralogy and Petrology* 169(6), pages 1–19. DOI: `10.1007/s00410-015-1144-5`.

Eilers, P. H. (2004). “Parametric time warping”. *Analytical Chemistry* 76(2), pages 404–411. DOI: `10.1021/ac034800e`.

Fiege, A., F. Holtz, H. Behrens, C. W. Mandeville, N. Shimizu, L. S. Crede, and J. Göttlicher (2015). “Experimental investigation of the S and S-isotope distribution between H_2O–S±Cl fluids and basaltic melts during decompression”. *Chemical Geology* 393, pages 36–54. DOI: `10.1016/j.chemgeo.2014.11.012`.

Fine, G. and E. Stolper (1985). “The speciation of carbon dioxide in sodium aluminosilicate glasses”. *Contributions to Mineralogy and Petrology* 91(2), pages 105–121. DOI: `10.1007/BF00377759`.

– (1986). “Dissolved carbon dioxide in basaltic glasses: concentrations and speciation”. *Earth and Planetary Science*

Letters 76(3-4), pages 263–278. DOI: 10.1016/0012-821X(86)90078-6.

Gelman, A. and D. B. Rubin (1992). “Inference from iterative simulation using multiple sequences”. *Statistical science*, pages 457–472. DOI: 10.1214/ss/1177011136.

Hauri, E., J. Wang, J. E. Dixon, P. L. King, C. Mandeville, and S. Newman (2002). “SIMS analysis of volatiles in silicate glasses: 1. Calibration, matrix effects and comparisons with FTIR”. *Chemical Geology* 183(1-4), pages 99–114. DOI: 10.1016/S0009-2541(01)00375-8.

Helo, C., M.-A. Longpré, N. Shimizu, D. A. Clague, and J. Stix (2011). “Explosive eruptions at mid-ocean ridges driven by CO2-rich magmas”. *Nature Geoscience* 4(4), pages 260–263. DOI: 10.1038/ngeo1104.

Hervig, R. L., G. Moore, and K. Roggensack (2009). “Calibrating carbon measurements in basaltic glass using SIMS and FTIR: The effect of variable H_2O contents”. In: *AGU Fall Meeting Abstracts*. Volume 2009, V51E–1755.

Hess, K. and D. B. Dingwell (1996). “Viscosities of hydrous leucogranitic melts: A non-Arrhenian model”. *American Mineralogist: Journal of Earth and Planetary Materials* 81(9-10), pages 1297–1300. DOI: 10.2138/am-1996-9-1031.

Howie, R., J. Zussman, and W. Deer (1992). *An introduction to the rock-forming minerals*. Longman London, UK. DOI: 10.1180/DHZ.

Ihinger, P., R. Hervig, and P. McMillan (1994). “Analytical Methods for Volatiles in Glasses”. *Reviews in Mineralogy and Geochemistry* 30, pages 67–121. DOI: 10.1515/9781501509674-008.

Jakobsson, S. (1997). “Solubility of water and carbon dioxide in an Icelandite at 1400°C and 10 kilobars”. *Contributions to Mineralogy and Petrology* 127(1-2), pages 129–135. DOI: 10.1007/s004100050270.

Jendrzejewski, N., T. W. Trull, F. Pineau, and M. Javoy (1997). “Carbon solubility in Mid-Ocean Ridge basaltic melt at low pressures (250–1950 bar)”. *Chemical Geology* 138(1-2), pages 81–92. DOI: 10.1016/S0009-2541(96)00176-3.

King, P., T. Vennemann, J. Holloway, R. Hervig, J. Lowenstern, and J. Forneris (2002). “Analytical techniques for volatiles: A case study using intermediate (andesitic) glasses”. *American Mineralogist* 87(8-9), pages 1077–1089. DOI: 10.2138/am-2002-8-904.

Krige, D. G. (1951). “A statistical approach to some basic mine valuation problems on the Witwatersrand”. *Journal of the Southern African Institute of Mining and Metallurgy* 52(6), pages 119–139. DOI: 10.10520/AJA0038223X_4792.

Lee, L. C., C. Liong, O. Khairul, and A. A. Jemain (2017). “Effects of baseline correction algorithms on forensic classification of paper based on ATR-FTIR spectrum and principal component analysis (PCA)”. *Pertanika Journal of Science and Technology* 25(3), pages 767–774.

Leschik, M., G. Heide, G. Frischat, H. Behrens, M. Wiedenbeck, N. Wagner, K. Heide, H. Geißler, and U. Reinholz (2004). “Determination of H_2O and D_2O contents in rhyolitic glasses”. *Physics and Chemistry of Glasses* 45(4), pages 238–251.

Lesher, C. E. and F. J. Spera (2015). “Thermodynamic and transport properties of silicate melts and magma”. In: *The Encyclopedia of Volcanoes*. Elsevier, pages 113–141. DOI: 10.1016/B978-0-12-385938-9.00005-5.

Lesne, P., B. Scaillet, M. Pichavant, G. Iacono-Marziano, and J.-M. Beny (2011). “The H_2O solubility of alkali basaltic melts: an experimental study”. *Contributions to Mineralogy and Petrology* 162(1), pages 133–151. DOI: 10.1007/s00410-010-0588-x.

Lin, L. I.-K. (1989). “A concordance correlation coefficient to evaluate reproducibility”. *Biometrics*, pages 255–268. DOI: 10.2307/2532051.

Lowenstern, J. B. (2001). “Carbon dioxide in magmas and implications for hydrothermal systems”. *Mineralium Deposita* 36(6), pages 490–502. DOI: 10.1007/s001260100185.

Lytle, M. L., E. H. Hauri, and K. A. Kelley (2023). *Volatile and trace elements in submarine glasses from global back-arc spreading centers*. Interdisciplinary Earth Data Alliance (IEDA). DOI: 10.26022/IEDA/112829.

Mandeville, C. W., J. D. Webster, M. J. Rutherford, B. E. Taylor, A. Timbal, and K. Faure (2002). “Determination of molar absorptivities for infrared absorption bands of H_2O in andesitic glasses”. *American Mineralogist* 87(7), pages 813–821. DOI: 10.2138/am-2002-0702.

McIntosh, I. M., A. R. Nichols, K. Tani, and E. W. Llewellin (2017). “Accounting for the species-dependence of the 3500 cm^{-1} H_2O_t infrared molar absorptivity coefficient: Implications for hydrated volcanic glasses”. *American Mineralogist: Journal of Earth and Planetary Materials* 102(8), pages 1677–1689. DOI: 10.2138/am-2017-5952CCBY.

Menke, W. (2018). *Geophysical data analysis: Discrete inverse theory*. Academic Press. DOI: 10.1016/B978-0-12-490920-5.X5001-7.

Mercier, M., A. Di Muro, N. Métrich, D. Giordano, O. Belhadj, and C. W. Mandeville (2010). “Spectroscopic analysis (FTIR, Raman) of water in mafic and intermediate glasses and glass inclusions”. *Geochimica et Cosmochimica Acta* 74(19), pages 5641–5656. DOI: 10.1016/j.gca.2010.06.020.

Mysen, B. (2022). *Mass Transport in Magmatic Systems*. Elsevier. DOI: 10.1016/C2019-0-03232-3.

Mysen, B. O. and P. Richet (2018). *Silicate glasses and melts*. Elsevier. DOI: 10.1016/C2018-0-00864-6.

Mysen, B. O. and D. Virgo (1980a). “Solubility mechanisms of carbon dioxide in silicate melts: a Raman spectroscopic study”. *American Mineralogist* 65(9-10), pages 885–899.

– (1980b). “The solubility behavior of CO_2 in melts on the join $NaAlSi_3O_8$- $CaAl_2Si_2O_8$-CO_2 at high pressures and temperatures: a Raman spectroscopic study”. *American Mineralogist* 65(11-12), pages 1166–1175.

– (1986). “Volatiles in silicate melts at high pressure and temperature: 1. Interaction between OH groups and Si^{4+}, Al^{3+}, Ca^{2+}, Na^{+} and H^{+}”. *Chemical Geology* 57(3-4), pages 303–331. DOI: 10.1016/0009-2541(86)90056-2.

Newman, S., E. Stolper, and R. Stern (2000). “H_2O and CO_2 in magmas from the Mariana arc and back arc systems”. *Geochemistry, Geophysics, Geosystems* 1(5). DOI: 10.1029/1999GC000027.

Newman, S., E. M. Stolper, and S. Epstein (1986). “Measurement of water in rhyolitic glasses; calibration of an infrared spectroscopic technique”. *American Mineralogist* 71(11-12), pages 1527–1541.

Nichols, A. R. and R. Wysoczanski (2007). “Using micro-FTIR spectroscopy to measure volatile contents in small and unexposed inclusions hosted in olivine crystals”. *Chemical Geology* 242(3-4), pages 371–384. DOI: `10.1016/j.chemgeo.2007.04.007`.

Nishikida, K., E. Nishio, and R. W. Hannah (1996). *Selected applications of modern FTIR techniques*. CRC Press. DOI: `10.1201/9780203739983`.

Nowak, M. and H. Behrens (1995). “The speciation of water in haplogranitic glasses and melts determined by in situ near-infrared spectroscopy”. *Geochimica et Cosmochimica Acta* 59(16), pages 3445–3450. DOI: `10.1016/0016-7037(95)00237-T`.

Ochs III, F. A. and R. A. Lange (1999). “The density of hydrous magmatic liquids”. *Science* 283(5406), pages 1314–1317. DOI: `10.1126/science.283.5406.1314`.

Ohlhorst, S., H. Behrens, and F. Holtz (2001). “Compositional dependence of molar absorptivities of near-infrared OH- and H_2O bands in rhyolitic to basaltic glasses”. *Chemical Geology* 174(1-3), pages 5–20. DOI: `10.1016/S0009-2541(00)00303-X`.

Okumura, S., M. Nakamura, and S. Nakashima (2003). “Determination of molar absorptivity of IR fundamental OH-stretching vibration in rhyolitic glasses”. *American Mineralogist* 88(11-12), pages 1657–1662. DOI: `10.2138/am-2003-11-1204`.

Okumura, S. and S. Nakashima (2005). “Molar absorptivities of OH and H_2O in rhyolitic glass at room temperature and at 400–600°C”. *American Mineralogist* 90(2-3), pages 441–447. DOI: `10.2138/am.2005.1740`.

Pandya, N., D. W. Muenow, and S. K. Sharma (1992). “The effect of bulk composition on the speciation of water in submarine volcanic glasses”. *Geochimica et Cosmochimica Acta* 56(5), pages 1875–1883. DOI: `10.1016/0016-7037(92)90317-C`.

Pearce, J. A., M. Ernewein, S. H. Bloomer, L. M. Parson, B. J. Murton, and L. E. Johnson (1994). “Geochemistry of Lau Basin volcanic rocks: influence of ridge segmentation and arc proximity”. *Geological Society, London, Special Publications* 81(1), pages 53–75. DOI: `10.1144/GSL.SP.1994.081.01.04`.

Peng, J., S. Peng, A. Jiang, J. Wei, C. Li, and J. Tan (2010). “Asymmetric least squares for multiple spectra baseline correction”. *Analytica Chimica Acta* 683(1), pages 63–68. DOI: `10.1016/j.aca.2010.08.033`.

Rasmussen, D. J. (2019). *The Aleutian Arc through and through: Subduction dynamics and the generation, storage, and eruption of hydrous magmas*. Columbia University. DOI: `10.7916/d8-vmrb-pf70`.

Savitzky, A. and M. J. Golay (1964). “Smoothing and differentiation of data by simplified least squares procedures”. *Analytical Chemistry* 36(8), pages 1627–1639. DOI: `10.1021/ac60214a047`.

Shi, S., A. Barth, T. Plank, W. Towbin, O. Flores, and C. Arias (2021). “Magma stalling weakens eruption”. In: *AGU Fall Meeting Abstracts*. Volume 2021, V25E–09.

Shishkina, T. A., R. E. Botcharnikov, F. Holtz, R. R. Almeev, A. M. Jazwa, and A. A. Jakubiak (2014). “Compositional and pressure effects on the solubility of H_2O and CO_2 in mafic melts”. *Chemical Geology* 388, pages 112–129. DOI: `10.1016/j.chemgeo.2014.09.001`.

Shishkina, T. A., R. E. Botcharnikov, F. Holtz, R. R. Almeev, and M. V. Portnyagin (2010). “Solubility of H_2O-and CO_2-bearing fluids in tholeiitic basalts at pressures up to 500 MPa”. *Chemical Geology* 277(1-2), pages 115–125. DOI: `10.1016/j.chemgeo.2010.07.014`.

Silver, L. A., P. D. Ihinger, and E. Stolper (1990). “The influence of bulk composition on the speciation of water in silicate glasses”. *Contributions to Mineralogy and Petrology* 104, pages 142–162. DOI: `10.1007/BF00306439`.

Silver, L. A. and E. Stolper (1989). “Water in albitic glasses”. *Journal of Petrology* 30(3), pages 667–709. DOI: `10.1093/petrology/30.3.667`.

Sisson, T. and T. Grove (1993). “Experimental investigations of the role of H_2O in calc-alkaline differentiation and subduction zone magmatism”. *Contributions to mineralogy and petrology* 113(2), pages 143–166. DOI: `10.1007/BF00283225`.

Stabile, P., E. Appiah, M. Bello, G. Giuli, E. Paris, and M. R. Carroll (2020). “New IR spectroscopic data for determination of water abundances in hydrous pantelleritic glasses”. *American Mineralogist* 105(7), pages 1060–1068. DOI: `10.2138/am-2020-7363`.

Stolper, E. (1982). “Water in silicate glasses: an infrared spectroscopic study”. *Contributions to Mineralogy and Petrology* 81(1), pages 1–17. DOI: `10.1007/BF00371154`.

– (1989). “Temperature dependence of the speciation of water in rhyolitic melts and glasses”. *American Mineralogist* 74(11-12), pages 1247–1257.

Sun, W., R. Binns, A. Fan, V. S. Kamenetsky, R. Wysoczanski, G. Wei, Y. Hu, and R. Arculus (2007). “Chlorine in submarine volcanic glasses from the eastern Manus basin”. *Geochimica et Cosmochimica Acta* 71(6), pages 1542–1552. DOI: `10.1016/j.gca.2006.12.003`.

Tamic, N., H. Behrens, and F. Holtz (2001). “The solubility of H_2O and CO_2 in rhyolitic melts in equilibrium with a mixed CO_2–H_2O fluid phase”. *Chemical Geology* 174(1-3), pages 333–347. DOI: `10.1016/S0009-2541(00)00324-7`.

Ter Braak, C. J. (2006). “A Markov Chain Monte Carlo version of the genetic algorithm Differential Evolution: easy Bayesian computing for real parameter spaces”. *Statistics and Computing* 16, pages 239–249. DOI: `10.1007/s11222-006-8769-1`.

Ter Braak, C. J. and J. A. Vrugt (2008). “Differential Evolution Markov Chain with snooker updater and fewer chains”. *Statistics and Computing* 18(435-446). DOI: `10.1007/s11222-008-9104-9`.

Thibault, Y. and J. R. Holloway (1994). “Solubility of CO_2 in a Ca-rich leucitite: effects of pressure, temperature, and oxygen fugacity”. *Contributions to Mineralogy and Petrology* 116, pages 216–224. DOI: `10.1007/BF00310701`.

Vetere, F., H. Behrens, F. Holtz, and D. R. Neuville (2006). "Viscosity of andesitic melts—new experimental data and a revised calculation model". *Chemical Geology* 228(4), pages 233–245. DOI: `10.1016/j.chemgeo.2005.10.009`.

Vetere, F., R. E. Botcharnikov, F. Holtz, H. Behrens, and R. De Rosa (2011). "Solubility of H_2O and CO_2 in shoshonitic melts at 1250°C and pressures from 50 to 400 MPa: implications for Campi Flegrei magmatic systems". *Journal of Volcanology and Geothermal Research* 202(3-4), pages 251–261. DOI: `10.1016/j.jvolgeores.2011.03.002`.

Vetere, F., F. Holtz, H. Behrens, R. E. Botcharnikov, and S. Fanara (2014). "The effect of alkalis and polymerization on the solubility of H_2O and CO_2 in alkali-rich silicate melts". *Contributions to Mineralogy and Petrology* 167, pages 1–17. DOI: `10.1007/s00410-014-1014-6`.

Von Aulock, F. W., B. M. Kennedy, C. I. Schipper, J. Castro, D. Martin, C. Oze, J. M. Watkins, P. J. Wallace, L. Puskar, F. Bégué, et al. (2014). "Advances in Fourier transform infrared spectroscopy of natural glasses: From sample preparation to data analysisdvances in Fourier transform infrared spectroscopy of natural glasses: From sample preparation to data analysis". *Lithos* 206, pages 52–64. DOI: `10.1016/j.lithos.2014.07.017`.

Withers, A. C. and H. Behrens (1999). "Temperature-induced changes in the NIR spectra of hydrous albitic and rhyolitic glasses between 300 and 100 K". *Physics and Chemistry of Minerals* 27(2), pages 119–132. DOI: `10.1007/s002690050248`.

Wysoczanski, R. and K. Tani (2006). "Spectroscopic FTIR imaging of water species in silicic volcanic glasses and melt inclusions: An example from the Izu-Bonin arc". *Journal of Volcanology and Geothermal Research* 156(3-4), pages 302–314. DOI: `10.1016/j.jvolgeores.2006.03.024`.

Xue, X. (2009). "Water speciation in hydrous silicate and aluminosilicate glasses: Direct evidence from ^{29}Si-^{1}H and ^{27}Al-^{1}H double-resonance NMR". *American Mineralogist* 94(2-3), pages 395–398. DOI: `10.2138/am.2009.3088`.

Yamashita, S., T. Kitamura, and M. Kusakabe (1997). "Infrared spectroscopy of hydrous glasses of arc magma compositions". *Geochemical Journal* 31(3), pages 169–174. DOI: `10.2343/geochemj.31.169`.